Bachelor Thesis
TU Delft, Faculty of Applied Sciences, BSc program Applied Physics

Behaviour of ODS 12Cr steel under thermal treatment at micro and macro level

A positron annihilation and Vickers hardness study

Author:
Friso Hoogenberg - 4551664

Supervisors:
Dr. H. Schut
V. Marques Pereira, MSc.

A thesis submitted in partial fulfilment of the requirements for the degree of

Bachelor of Science
in
Physics

in the section

Neutron and Positron Methods in Materials
Radiation Science & Technology

Delft
July 5, 2019

Abstract

The behaviour of ODS 12Cr steel under thermal treatment is studied in this report at micro and macro level. ODS 12Cr steel is always in the ferrite phase and has a melting point at 1500 °C. Before studying, the retrieved samples were metallographically prepared in four steps: mounting, grinding, mechanically polishing and electrolytically polishing. A measurement was done to analyse the effect of electrolytically polishing on bulk S and W parameters. This showed that mechanically polishing with 0.04 μm alumina particles has the same effect as electrolytically polishing. Next, the alloy was studied with three different measurement techniques: positron annihilation Doppler broadening spectroscopy, Vickers hardness test and positron lifetime measurements. Before these measurements the samples were annealed at selected temperatures for 10 minutes and naturally cooled.

The Doppler broadening spectroscopy was done with the Variable Energy Positron beam (VEP) at the Reactor Institute Delft (RID). With this set-up the S and W parameter were measured at different implantation energies and converging bulk values of them were determined. The results were fitted with VEPFIT. This measurement was done in the as received state and after annealing from 200 °C up to 1300 °C in steps of 100 °C. The Vickers hardness test was done with a load of 0.3 kgf and in the same temperature range as the VEP measurements but with steps of 200 °C. A lifetime spectrum was measured in the as received state with two sample sandwiching a ^{22}Na source packed with kapton. The average lifetime was determined by fitting the spectrum with LT 9.2. This measurement was repeated after annealing for 10 minutes from 200 °C up to 700 °C in steps of 100 °C.

The three different measurement techniques show corresponding results. Up to annealing temperatures of 1000 °C the results stay constant. The bulk S and W parameters are respectively 0.475 and 0.078. The Vickers hardness stays at 395 HV and is comparable to literature values. The average lifetime is approximately 208 ps, which corresponds with defects with sizes comparable to or at least larger than that of divacancies. At this temperatures most thermal vacancies are trapped by the nano-oxide particles and are not able to liberate themselves which causes the constant results. At higher temperatures (larger than 1100 °C) the thermal vacancy concentration increases and the vacancies gain enough energy to be liberated. This causes, in combination with oxide particles clustering, more defects in the material and explains the increasing bulk S value for temperatures up from 1100 °C. The high bulk S values, compared with an iron alloy with less chromium, can also originate from clustering of chromium atoms. The surface S parameters are also increased in this temperature domain due to the formation of an oxide layer which can be seen with the naked-eye. Finally, the hardness value decreases to 374 HV after annealing at 1200 °C which is a significant decrease and indicates that the pinning of the nano-particles decreases, resulting in grains growing easier.

Contents

Chapter 1

Introduction

Nuclear reactors create extreme conditions like irradiation and high temperatures in which fission and fusion take place. These extreme conditions impose strong requirements on the materials used to build such reactors. Oxide dispersion strengthened (ODS) ferritic steels have been mentioned as good candidates as first walls in future reactors [1], because of their stability under irradiation [2]. Beside its irradiation resistance, ODS steels have a high creep strength which makes it withstand high temperatures [1]. The oxide particles present in ODS steels play in both advantages a main role. These particles trap defects like vacancies created by irradiation [3] and decrease movement of dislocations [4]. To use specific ODS steels in nuclear reactors the behaviour of the alloy at high temperatures has to been known. Therefore, ODS 12Cr steel is studied in this research under thermal treatment at micro and macro level.

At micro level the type and occurrence of defects is studied as well as the operation of the oxide particles. This is done with positron annihilation, because positrons interact with defects. In defect free material positrons are repelled by the nuclei in the crystal lattice and therefore are located in between the atoms. When defects are present, it is more favourable for positrons to locate at those positions. Due to a lower electron density in defects, positrons will live longer than in defect free material. The lifetime of positrons is a measure for the type of defects present. Beside lifetime measurements, Doppler broadening spectroscopy is used to gain a measure of the defect concentration. At macro level the Vickers hardness of ODS 12Cr steel is measured to see the degree of plastic deformation. These three measurements are done after annealing stages at different temperatures up to 1300 °C.

In chapter 2 of this report the underlying theory of the experiment is described. The following chapters, 3, 4, 5 and 6, are respectively the experimental method, the results, the discussion and the conclusion.

This research was conducted in partial fulfilment of the requirements for the degree of Bachelor of Science in Physics at the Delft University of Technology within the faculty of Applied Sciences.

Chapter 2

Theory

2.1 Positron annihilation

Positron annihilation is the process where an electron and its antiparticle, a positron, combine and produce electromagnetic radiation. The number of produced photons can vary. In this research only two photon creation is considered, because it is the most common case. The annihilation rates for the creation of other numbers of photons are much smaller, for example, the rates for the creation of one and three photons scale respectively with α^4 and α, where α is the fine structure constant [5]. The two photon creation positron annihilation reaction is given by

$$e^- + e^+ \rightarrow \gamma + \gamma \, . \tag{1}$$

To study positron annihilation the relation between the energies and momenta of the photons, electron and positron should be known. These can be found using the conservation laws of energy and momentum. In figure 1a a schematic representation of the situation before the annihilation is shown. When the positron is inside the material and has lost its energy (thermalized), its momentum can be neglected. For simplicity the positron is chosen in the origin. The electron is coming in with momentum $\vec{p}_e$, which makes an angle ϕ with the negative x-axis. The x- and y-component of the electrons momentum are respectively $\vec{p}_x$ and $\vec{p}_y$. The situation after the annihilation is shown in figure 1b, where $\vec{p}_{ph,1}$ and $\vec{p}_{ph,2}$ are respectively the momenta of the first and second photon. The second photon makes a small angle θ with the negative x-axis.

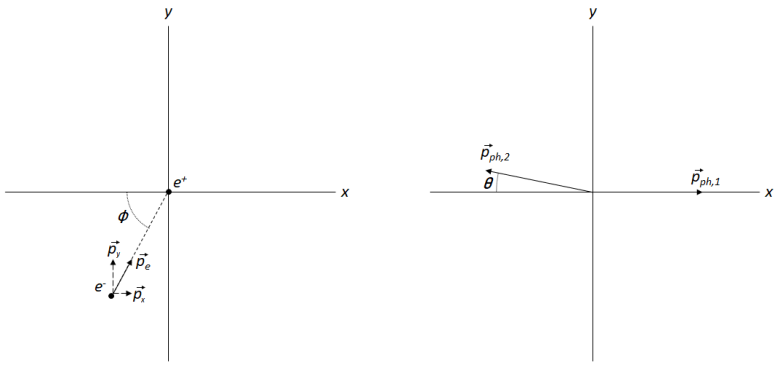

(a) (b)

Figure 1: (a) Situation before annihilation. The electron is coming in with momentum $\vec{p}_e$ with an angle ϕ with the negative x-axis, while the positron is in the origin. The momentum of the electron can be factorised in $\vec{p}_x$ and $\vec{p}_y$. (b) Situation after annihilation. Two photons are emitted with momenta $\vec{p}_{ph,1}$ and $\vec{p}_{ph,2}$. The second photon makes an angle θ with the negative x-axis.

When applying the conservation laws for energy and momentum the following equations are retrieved

$$\begin{cases} \sqrt{m_0^2c^4 + p_e^2c^2} + m_0c^2 & = E_{ph,1} + E_{ph,2} \\ cp_x & = E_{ph,1} - E_{ph,2}\cos(\theta) \\ cp_y & = E_{ph,2}\cos(\theta) \end{cases}, \tag{2}$$

where m_0 is the rest mass of the electron and positron, c the speed of light in vacuum and $E_{ph,1}$ and $E_{ph,2}$ the energies of the first and second photon, respectively. Solving this set of equations for θ, $E_{ph,1}$ and $E_{ph,2}$ results in

$$\begin{cases} \theta & = \frac{2p_yc}{p_xc+m_0c^2+\sqrt{m_0^2c^4+p_e^2c^2}} \\ E_{ph,1} & = \frac{m_0c^2+\sqrt{m_0^2c^4+p_e^2c^2}+p_xc}{2} \\ E_{ph,2} & = \frac{m_0c^2+\sqrt{m_0^2c^4+p_e^2c^2}-p_xc}{2} \end{cases}. \tag{3}$$

The kinetic energy of the electron is small compared with its rest mass energy and therefore $p_ec \ll m_0c^2$ is assumed. This simplifies the set of equations into

$$\begin{cases} \theta & = \frac{p_y}{m_0c} \\ E_{ph,1} & = m_0c^2 + \frac{1}{2}p_xc \\ E_{ph,2} & = m_0c^2 - \frac{1}{2}p_xc \end{cases}. \tag{4}$$

Due to energy and momentum conservations two techniques are established to study positron annihilation. The first equation in (4) states that the angle between the photons depends on the perpendicular momentum component of the electron. The second and third equation together show the energy shifts depending on the parallel momentum component of the electron. The technique that uses this energy shift is called Doppler broadening spectroscopy and is used in this research to study the annihilation of positrons.

2.2 Positron annihilation Doppler broadening spectroscopy

In Doppler broadening spectroscopy the energy of the annihilation photons is measured for a large number of annihilation events. These energies are plotted in a histogram called a gamma spectrum. To analyse the gamma spectrum and indirectly the initial electron and positron, two parameters are defined: the S parameter and the W parameter. In figure 2 a gamma spectrum is shown and the areas corresponding with these parameters are marked. The S and W parameter are respectively called the "shape" and "wing" parameter. The amount of annihilation events with valance or conduction electrons, i.e., low-momentum electrons is quantitatively measured with the S parameter. The W parameter on the other hand is a measure for the amount of annihilation events with high-momentum electrons, i.e., core electrons. The S and W parameter are calculated by dividing the area of the central part of the peak and the area under the wing of the peak by the total area of the peak, respectively. This results in the following equation for the S parameter

$$S = \frac{A_S}{A_0}, \tag{5}$$

with A_S the area of the low-momentum part of the spectrum and A_0 the total area below the curve. The W parameter is obtained similarly

$$W = \frac{A_W}{A_0}, \tag{6}$$

with A_W the area under the wing of the peak [6].

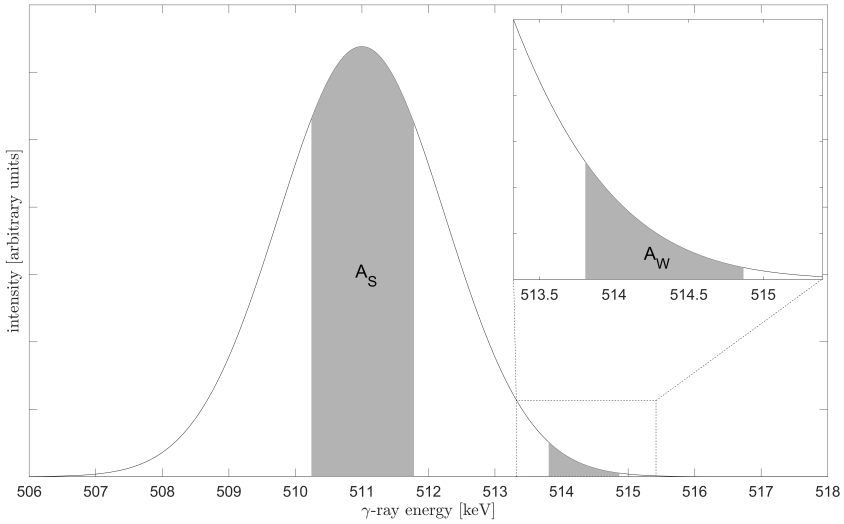

Figure 2: Gamma spectrum with the areas A_S and A_W marked. To show A_W clearer a subplot is made zoomed in around this area.

Note that the area A_S is symmetrically chosen around 511 keV. It is a convention to choose the boundaries of the S parameter such that S equals 0.5 for a defect-free material. This makes it most sensitive for defects. The width of the area A_S and A_W should be kept constant for different spectra to make them comparable. To be sure that the W parameter and the S parameter have no correlation, the boundaries of the area A_W should not overlap with the area A_S. The conventional W equals $0.25 \cdot S$ [6].

The S and W parameter values can be correlated to the types of defects present in the analysed material. In open volume defects the electron density is lower than in defect free parts of the material. The free electrons present in these defects have low momenta and therefore the S parameter depends on the concentration of defects. When there are more open volume defects the S parameter will be higher and vice versa. The W parameter on the other hand carries information about the local chemical surrounding of the trapping annihilation site due to the annihilation with core electrons, i.e., high-momentum electrons.

2.3 Positron behaviour in material

Inside matter positrons can behave in various ways. An overview of the possible interactions of positrons in matter is shown in figure 3. At the surface positrons have two options: being back-scattered (diffracted) or entering the material. After entering the material, the positrons interact with the electrons and nuclei present. They lose energy due to the excitation of core electrons and the scattering with conduction electrons. This energy loss continues until they have lost all their kinetic energy and are in thermal equilibrium with the material ('thermalized'). Thermalized positrons can diffuse through the material which results in positrons leaving the material again, but also in annihilation events with electrons. The back-diffused positrons can leave the material in different ways: as slow positrons, as epithermal positrons (high energy) or as positronium.

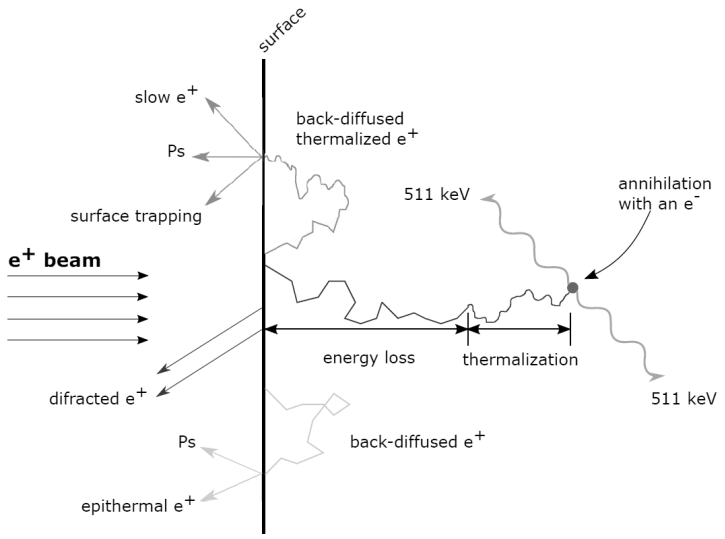

Figure 3: Overview of the different interactions of positrons in materials. This image is modified from [7].

2.3.1 Makhov distribution

In materials positrons lose their energy before annihilation. Therefore, the implantation energy is a measure for the penetration depth of positrons in materials. The relation between implantation energy and penetration depth can be obtained from the transmission probability [8]:

$$\eta_T(z, E) = e^{-\left(\frac{z}{z_0}\right)^m}, \tag{7}$$

with z the penetration depth, E the implantation energy, m a dimensionless empirical parameter and z_0 defined as [8]

$$z_0 = \frac{\bar{z}}{\rho\Gamma\left[\frac{1}{m}+1\right]}, \tag{8}$$

with $\bar{z}$ the mean implantation depth, ρ the density of the material and Γ the gamma function. The mean implantation depth is defined by [8]

$$\bar{z} = \frac{\alpha}{\rho}E^n. \tag{9}$$

In this equation the empirical parameters have typical values: $n = 1.62$, $m = 2$ and $\alpha = 4.0$ μg cm^{-2} keV^{-n} [6].

To get the implantation profile, i.e. the Makhov distribution, the absolute value of the derivative of equation 7 has to be taken, resulting in

$$P(z, E) = \frac{mz^{m-1}}{z_0^m}e^{-\left(\frac{z}{z_0}\right)^m}. \tag{10}$$

Four examples of the implantation profile of positrons in iron are calculated using equation 10 and plotted in figure 4. The vertical lines represent the mean implantation energies for the different Mahkov profiles. Note that the profiles become wider with increasing implantation energies.

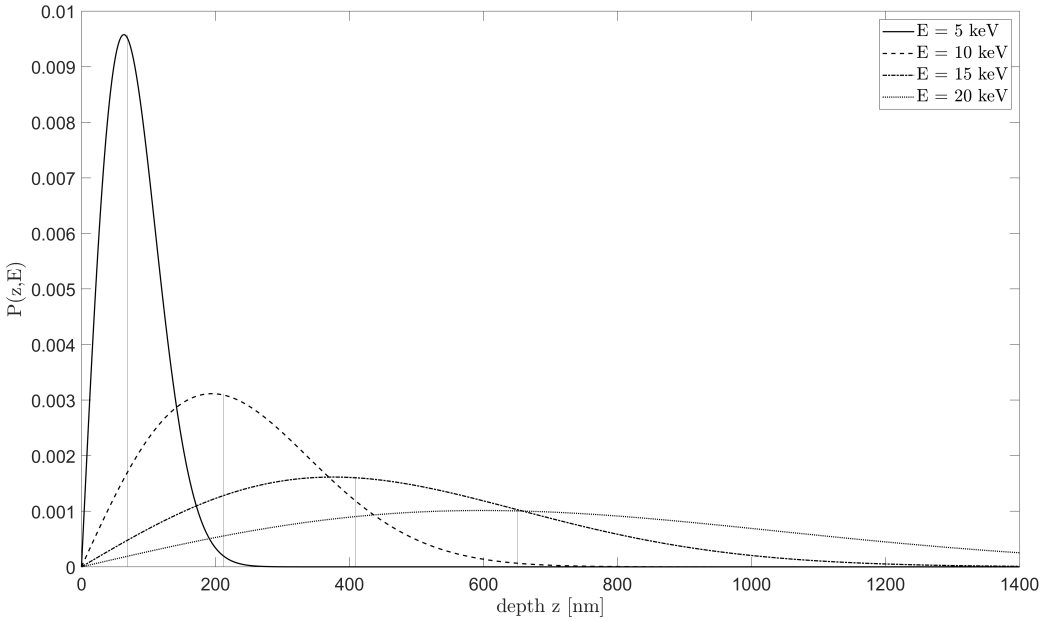

Figure 4: Mahkov depth profiles for different energies in iron. The vertical lines represent the mean implantation energy for the different implantation energies.

2.3.2 Diffusion of positrons

First, positrons lose their energy mainly by scattering with conduction electrons. When their energy is below 1 eV, scattering with phonons becomes the main contribution. This process of thermalization happens rapidly and therefore diffusion is the dominant event of the positron lifetime.

Diffusion of thermalized positrons is mainly affected by the Coulomb interactions with the nuclei present in the crystal structure. In a defect free material there is a periodic potential due to the nuclei present at lattice points. The lowest potentials are located in the interstices between atoms, as schematically shown in figure 5. Therefore, it is most favourable for positrons to be located in between the nuclei.

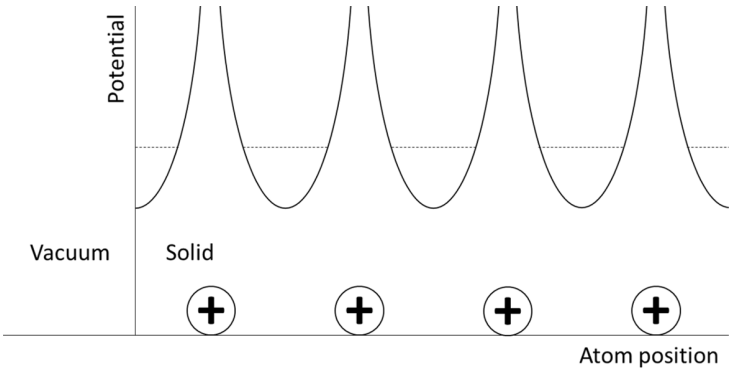

Figure 5: Potential felt by a positron travelling through a defect free lattice. The dashed horizontal lines represent the positron energy inside the potential.

When defects are present in the material, like vacancies, the potential felt by the positrons changes. A vacancy is a type of point defect, and is intrinsic to materials. It forms when an atom is displaced, or removed, from its lattice position. So, in lattice sites where atoms are missing, the Coulomb potential will show a minimum, becoming preferable sites for

positron occupation. Positrons can be trapped in these potential wells and are bound to it with the binding energy defined as the difference between the energy level in the vacancy and the energy level in the neighbouring potential minima. In figure 6 such a potential is schematically shown.

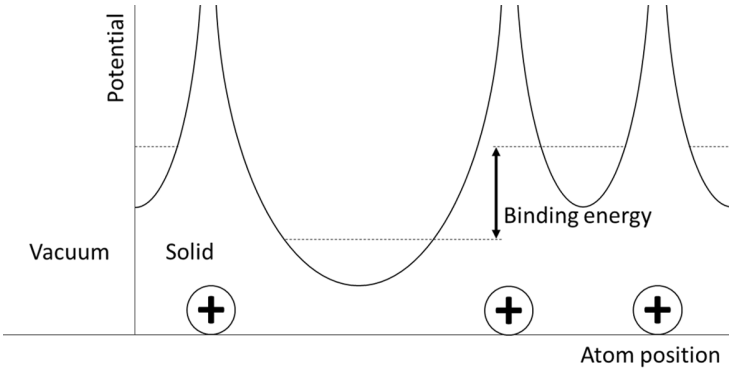

Figure 6: Potential felt by a positron travelling through a lattice with defects. The dashed horizontal lines represent the positron energy inside the potential and the vertical arrow shows the binding energy.

Based on the trapping of positrons, as discussed, a diffusion equation for positrons inside a material containing defects can be derived. This one dimensional steady-state diffusion equation equals [9]:

$$D^{+}\frac{d^2c(z)}{dz^2} - \frac{d}{dz}\left(v_d(z)c(z)\right) + I(z) - k_t n_t(z)c(z) - \lambda_b c(z) = 0\,, \tag{11}$$

with

D_+	=	the positron diffusion coefficient,
$c(z)$	=	the steady state positron distribution,
$v_d(z)$	=	$\mu E(z)$ = the positron drift velocity,
$E(z)$	=	the electric field strength,
μ	=	eD_+/k_BT = the positron mobility,
$I(z)$	=	the energy dependent positron implantation rate,
k_t	=	the specific positron trapping rate for defects,
$n_t(z)$	=	the defect concentration, and
λ_b	=	the bulk annihilation rate.

In this research the second term will be zero, because no electric field is present. To get the diffusion of positrons the differential equation has to be normalized and integrated over the implantation depth. This results in

$$F_s + F_t + F_b = 1\,, \tag{12}$$

with F_S the fraction of positrons diffusion back to the surface, F_t the fraction of positrons that get trapped and F_b the fraction of positrons that annihilate in the bulk. These three fractions sum up to one, because no positrons are lost in theory. In reality positrons form positronium or can be emitted as epithermal positrons which lowers the sum of the three fractions. These effects are discussed in the next paragraphs.

In this research the diffusion equation is solved with the fitting software VEPFIT (see paragraph 3.3.3), in order to analyse the results obtained with the Doppler broadening spectroscopy.

2.3.3 Annihilation states

After thermalization, positrons can annihilate in different ways as shown in figure 7.

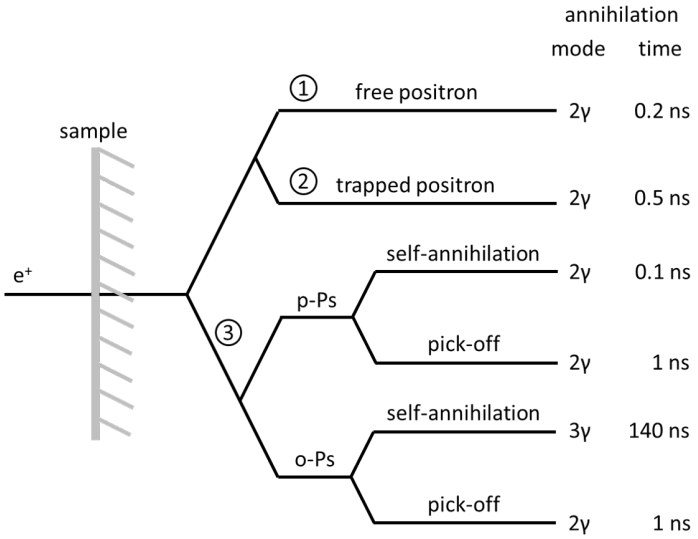

Figure 7: Possible annihilation states of thermalized positrons in material including their mode and lifetime.

The first option is annihilation when the positron is located interstitially. The positron can move freely and can annihilate in this mode with conduction, valance and core electrons. When annihilating with a core electron the W parameter will be high, because of its high momentum.

A different option is the annihilation as a trapped positron (number 2 in figure 7). Trapped positrons are located inside defects where nuclei are missing. Therefore, less core electrons are present and the positron mainly annihilates with free electrons. Those electrons have low energies and thus the S parameter will be higher.

Other type of annihilation states (number 3 in figure 7) are related to the formation of positronium. Positronium is a bound combination of an electron and a positron and is similar to a hydrogen atom [10]. It can be formed at the surface of the material with back-diffused positrons, which can be thermalized or non-thermalized [11], see figure 3. Two types of positronium are known depending on their relative spin: para-positronium (p-Ps), in the singlet spin state, and ortho-positronium (o-Ps), in the triplet spin state. Because positronium is not a stable state, it can self-annihilate. Free p-Ps in vacuum emits after self-annihilation an even number of photons, with two as most probable ($\tau \approx 125$ ps), while o-Ps emits an odd number (one not possible, three or higher) of photons ($\tau \approx 142$ ns) [12]. In materials, the positronium can react in two ways before annihilation: spin exchange with an electron (equation 13) and pick-off (equation 14). Because p-Ps has no internal momentum, the photons emitted have both 511 keV and can be detected with Doppler broadening spectroscopy. Since positronium formation happens only at the surface, this does not influence this research since the bulk values are studied.

$$\text{o-Ps}\,(\uparrow\uparrow) + e^-\,(\downarrow) \rightarrow \text{p-Ps}\,(\uparrow\downarrow) + e^-\,(\uparrow) \tag{13}$$

$$\text{o-Ps}\,(\uparrow\uparrow) + e^-\,(\downarrow) \rightarrow 2\gamma + e^-\,(\uparrow) \tag{14}$$

2.4 Positron annihilation lifetime

The lifetime of a positron is dependent on the electron density. When more electrons are present, the chance to annihilate increases and therefore the lifetime decreases and vice versa. This is described as

$$\lambda = \frac{1}{\tau} = \pi r_0^2 c n_e \,, \tag{15}$$

with λ the annihilation rate, τ the positron lifetime, r_0 the classical electron radius, c the speed of light and n_e the electron density. As explained, the electron density in open-volume defects is lower than in the surrounding, resulting in positrons living longer. Therefore, positron lifetime is a measure for the type of defects, determined by its "volume". The diffusion length of positrons determines the sensitivity of positrons to detect defects, because it is a measure for the number of atoms probed for positron traps [6].

Conventional positron lifetime measurements are done with ^{22}Na since it emits a 1274 keV photon just after the birth of a positron. During annihilation two photons of 511 keV are created marking its death. By measuring the time difference between the detection of these photons, the lifetime is obtained. A lifetime spectrum may consist of several lifetime components: free annihilation and one or more defect related annihilations. The intensity of each component is a measure for the concentration of the particular defect. The specific set-up used in this research is described in paragraph 3.5.1.

2.5 Material defects

Materials can have different type of defects. In this study vacancies, void, dislocations, grain boundaries and interfaces of carbides or oxide with the matrix are treated. The first three are schematically shown in figure 8

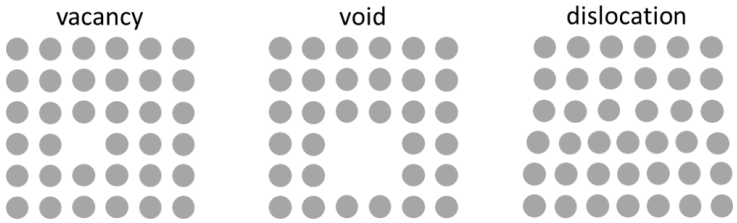

Figure 8: Three type of open-volume defects shown schematically: a vacancy, a void and a dislocation.

The simplest defect is a vacancy, which is a open-volume defect where one atom is removed from the crystal structure. A void is a large hole present in the crystal due to multiple nuclei missing near each other, i.e., a cluster of vacancies. In defect free crystals, planes of atoms are perfectly stacked on each other. A dislocation is a defect where an extra half-plane of atoms is stacked in between two planes as shown in figure 8.

Vacancies are intrinsic to materials and are present at every temperature above absolute zero. The equilibrium concentration of vacancies N_v is given by [13]:

$$N_v = N e^{\frac{-Q_v}{kT}} \,, \tag{16}$$

with N the total number of atomic sites ($N = 8.48 \cdot 10^8$ m^{-3} for pure iron), Q_v the energy required for the formation of a vacancy ($Q_v = 1.6$ eV [14]), k the Boltzmann's constant and T the temperature in K. In figure 9 this equilibrium relation between thermal vacancies and temperature for iron in the alpha phase is plotted.

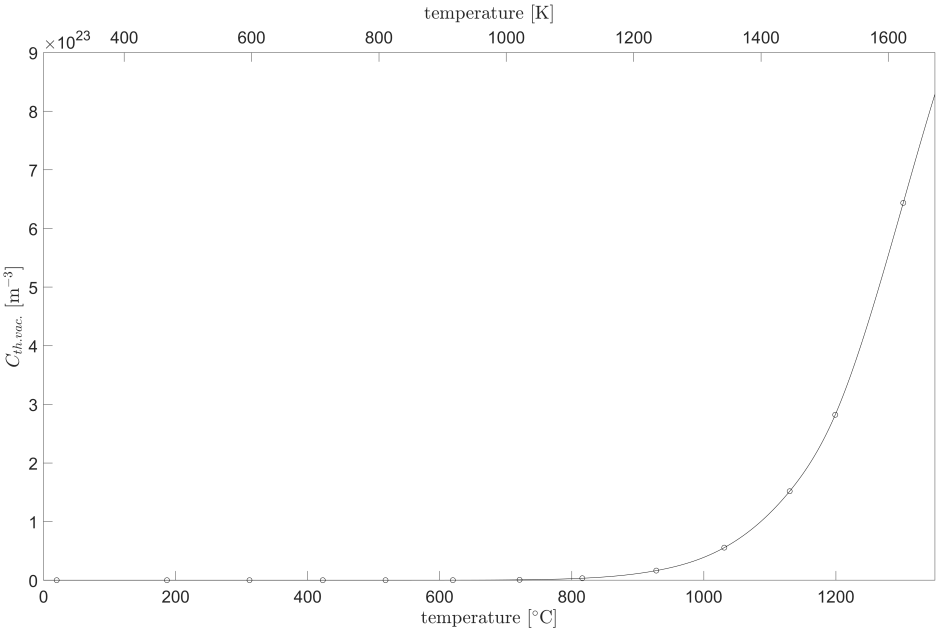

Figure 9: Equilibrium density of thermal vacancies in pure iron at different annealing temperatures.

An other type of defect are grain boundaries. Metals are not made of one single crystal, but many small ones called grains. Boundaries between grains are atomic mismatches and are therefore a type of defect. For example, small open volume can be present at those boundaries. The grains can move and deform due to stresses and temperature influencing the hardness of the material. At the grain boundaries carbides can be present, which create more sides of atomic mismatches and therefore increases the number of defects. Not only carbides but also other compounds can be present like oxide particles.

2.6 Oxide dispersion strengthened steels

Oxide dispersion strengthened (ODS) steels are steels with nano-oxide particles present in the matrix. The production of ODS steels is based on mechanical alloying. Pre-alloyed metallic powders are mixed with Y_2O_3 and ball-milled to allow a homogeneous distribution of the oxide particles in the matrix. Next, the alloy is consolidated by extrusion, plasma assisted sintering or hot isostatic pressing. Finally, thermo-mechanical treatments are done like hot and cold rolling. The mechanical alloying step mainly determines the microstructure in the ODS steel [15].

The nano-oxide particles present in ODS steels trap defects resulting in improved material properties. For example, vacancies can be trapped by an oxide particle, which reduced it freedom to diffuse. Dislocations are also trapped by the nano-oxide particle which improve the high-temperature strength [16]. When dislocations are trapped, the dominant way of passing is by climbing. Climbing is the process when dislocations move out of their plane of atoms and climb into the plane above or beneath them. This process is energetically unfavourable and therefore only happens at high temperatures. Besides forcing the dislocation to move only be climbing, oxide particles can pin dislocations even after climbing which is called interfacial pinning [17].

Finally, the oxide particles pin grain boundaries. Due to temperature the grains can move with respect to each other making the material easier to deform. The nano-oxide particles present in ODS steels prevents this by pinning them together during the temperature exposition [18].

Chapter 3

Experimental method

3.1 The samples

In this research two ODS 12Cr steel samples (15 x 15 x 1 mm) are used. They are cut from a bar produced by the Kobelco Research Institute in Japan. The production process and chemical composition are unfortunately not known. A possible production sequence includes mechanical alloying of metal powders and Y_2O_3 by ball milling, followed by canning, degassing, hot extrusion, hot forging and annealing [19].

To obtain the chemical composition and micro structural properties the received bar is cut in smaller samples and has been studied using a compositional analysis, Vickers hardness measurements and electron backscatter diffraction (EBSD). The hardness measurements showed that the hardness value was 395 HV and approximately uniform over the whole sample. The found chemical composition is shown in table 1.

Table 1: Chemical composition of the ODS 12Cr steel in weight percentage.

ODS 12Cr	**Fe**	**C**	**Cr**	**W**	**Ti**	**Zn**	**Y**	**Si**	**S**	**Al**
	85.082	0.03	12.292	1.719	0.303	0.040	0.144	0.170	0.040	0.126

ODS Cr steels can have different type of phases depending on the weight percentage chromium present in the alloy. In figure 10 the equilibrium phase diagram of this ODS 12Cr steel, made with Thermo-Calc software version 2018a, is shown. This phase diagram was obtained with the use of the TCFE9: Steels/Fe-alloys v9.0 database and the composition: Fe-0.03C-12.3Cr-0.3Ti-1.72W. It can be seen that steels with a chromium weight percentage of approximately 12 do not change phase during annealing, it stays in a body centred cubic (BCC) lattice structure (α phase) up to 1500 °C. The titanium carbides (TiC) at the grain boundaries disappear around 1300 °C and the Laves phases disappear between 400 and 500 °C.

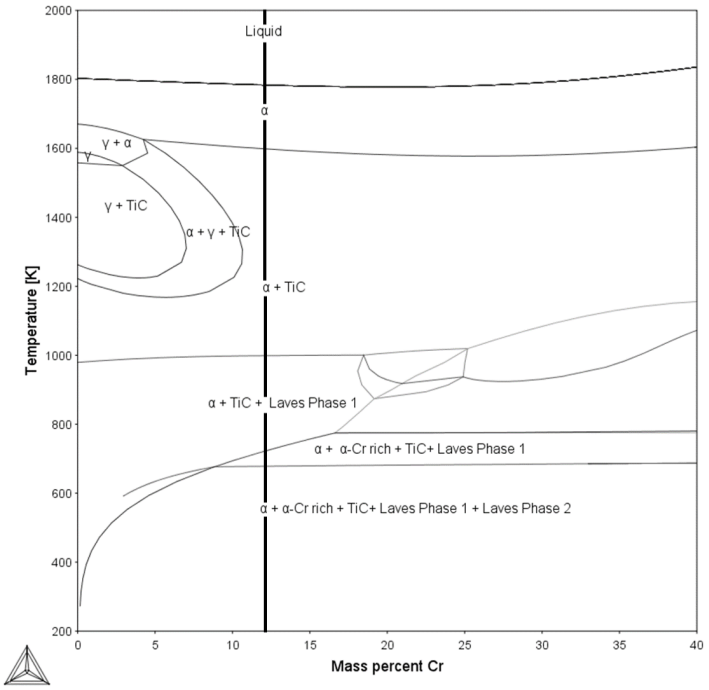

Figure 10: Equilibrium phase diagram of ODS Cr steels, made with Thermo-Calc version 2018a. The thick vertical line indicates the phase transitions of the ODS 12Cr steel used in this research. Composition used in Thermo-Calc: Fe-0.03C-12.3Cr-0.3Ti-1.72W; database selected TCFE9: Steels/Fe-alloys v9.0.

The phase diagram shown in figure 10 is only valid in equilibrium. However, the material will not be in equilibrium during this research, because some phase formations take a long time. Therefore, the Laves phases and the α-Cr rich phase are neglected in the calculations of the molar fractions. The results of this calculation can be found in figure 11. In this figure the analytical molar fractions of ferrite, titanium carbides (TiC) and liquid present in the samples are plotted versus temperature. In the insert in figure 11 the low molar fraction of the titanium carbides (FCC A1) is shown. Note that the molar faction stays approximately constant until 1300 K.

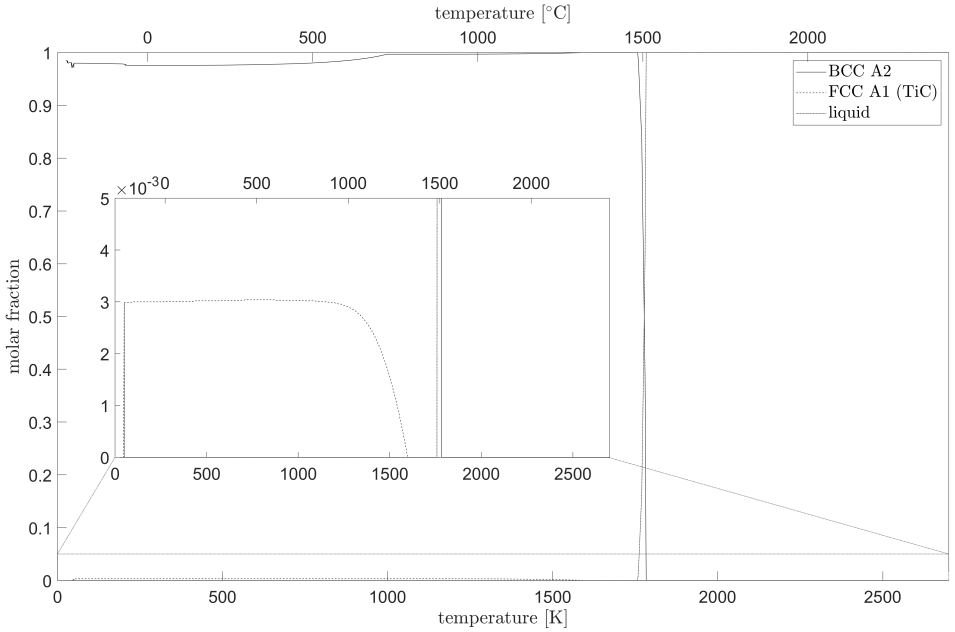

Figure 11: Molar fraction of relevant phases in equilibrium conditions of ODS 12Cr steel.

3.1.1 Sample preparation

One of the two received samples was used for Doppler broadening measurements, while the other was cut into three pieces with the Struers Secotom-10 using a diamond wafering blade. The cutting resulted in a small bar for hardness measurements and two equivalent samples for lifetime measurements. In figure 12 all the samples are schematically shown.

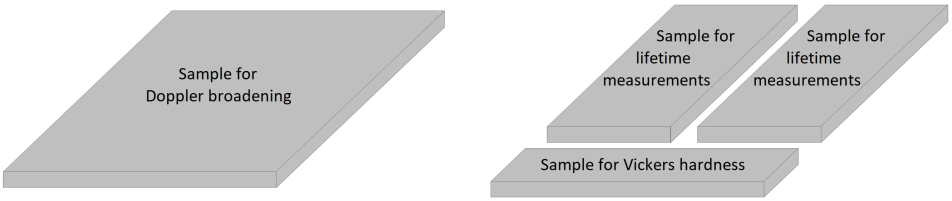

Figure 12: Schematic representation of all the samples used in this research. The right one has been cut into three pieces.

After cutting, the three cut samples and the uncut sample were metallographically prepared. The used metallographic preparation consisted of four steps: mounting, grinding, mechanically polishing and electrolytic etching.

First, the samples were mounted in PolyFast, a black bakelite hot mounting resin with carbon filler from Struers, using the Struers LaboPress-3. The compressive mounting took place at 180 °C for 10 minutes under a pressure of 25 kN. Afterwards the sample was cooled for 6 minutes. Figure 13 shows the mounting cylinder with at one end a sample.

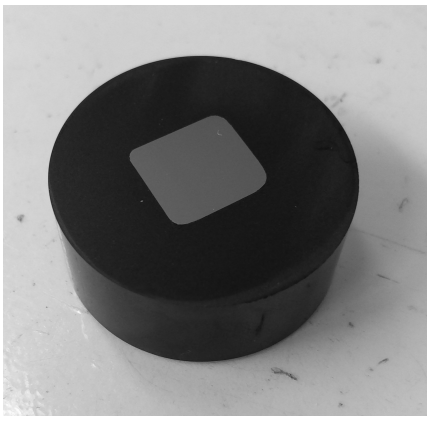

Figure 13: One of the samples mounted in PolyFast.

Next, the mounted samples were ground with different types of sandpaper using the Struers LaboPol-21 to obtain a flat surface. Chronologically, sandpapers with a grid number of 800, 1200 and 2000 with respectively a particle size of 21.8 μm, 15.2 μm and 10 μm were used. The samples were ground until scratches from the previous paper were removed. To distinguish scratches from different sandpapers the samples were turned 90 degrees when switching sandpapers. To minimise the heat-generated damage and metal entrapment between abrasive particles, water was used as lubricant and coolant.

Subsequently, the Struers TegraPol-11, TegraDoser-5 and TegraForce-1 were used to mechanically polish the samples. This was done to obtain a high reflective scratch-free surface by removing the scratches produced during grinding. Like with grinding the samples were polished in multiple steps, starting with a diamond suspension with a particle size of 3 μm for 9 minutes. Thereafter, a different diamond and a neutral alumina suspension were

used with respectively a particles size of 1 μm for 20 minutes and 0.04 μm for 30 minutes. During the polishing the TegraForce-1 pressed the samples with 10 N against the at 150 rpm spinning cloth of the TegraPol-11.

After each polishing step, the samples were cleaned using detergent, water and isopropanol and dried by a hair dryer to remove droplets. The cleaned samples were checked for scratches with the use of the dark field of the Olympus BX60M light microscope. When the scratches from the previous step were removed, the polishing suspension was switched for a finer one. The samples were cleaned extra after using the finest suspension. This was done by pushing them against the polishing cloth for 20 seconds with water as lubricant.

Finally, the bakelite mountings were broken using a workbench screw. Afterwards, two samples were electrolytically etched. One of the equally sized ones was not etched to measure the result of electrolytic etching. Also the small bar was not etched, because it does not influence the hardness measurements. The samples were connected to the positive pole of a power supply and a platinum electrode was connected to the negative one. These were embedded in a solution of 600 mL of distilled water with 6 grams of oxalic acid dissolved in it. The backside of the samples were protected by adhesive tape. The current used was 0.1 A for both samples and the voltage 4V. The uncut sample was etched for 16 minutes while one of the cut samples was etched for 5 minutes, because of the smaller surface. After the etching, the samples were cleaned in the same way as before using detergent, water and isopropanol.

3.2 Annealing

Samples of the ODS 12Cr steel were annealed at different temperatures, in order to evaluate its microstructural stability and evolution of defects. The annealing took place in a small oven, which is inside a vacuum chamber. A schematic representation of the annealing set-up is shown in figure 14. Two pumps, a roughing and a turbo pump, create a vacuum of the order of 10^{-6} mbar. The oven is heated by a tungsten coil which is connected to a current source which can be varied. Inside the coil, the samples are placed on a ceramic plate. This is surrounded by a molybdenum heat shield.

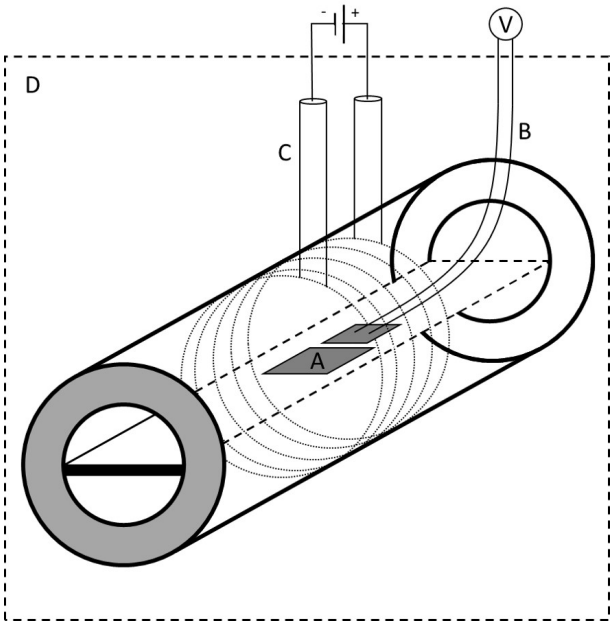

Figure 14: Schematic representation of the set-up used for annealing the samples. The sample is placed in the centre of the oven (A). (B) represents a reference sample with a thermocouple spot welded onto it, to determine the temperature. The coil and the current source that heat the oven are indicated by (C). The whole system was placed inside the vacuum chamber (D).

To monitor the temperature a reference sample is located in the middle of the oven onto which one side of a WRe 3/25 (type D) thermocouple is spot welded. The other end of the thermocouple is outside of the vacuum. The potential difference between both ends of the thermocouple is measured by a digital multimeter and by the use of a low and high temperature fit from earlier measurements. This potential difference is converted into a temperature difference. The fits are shown in figure 15 and equation 17:

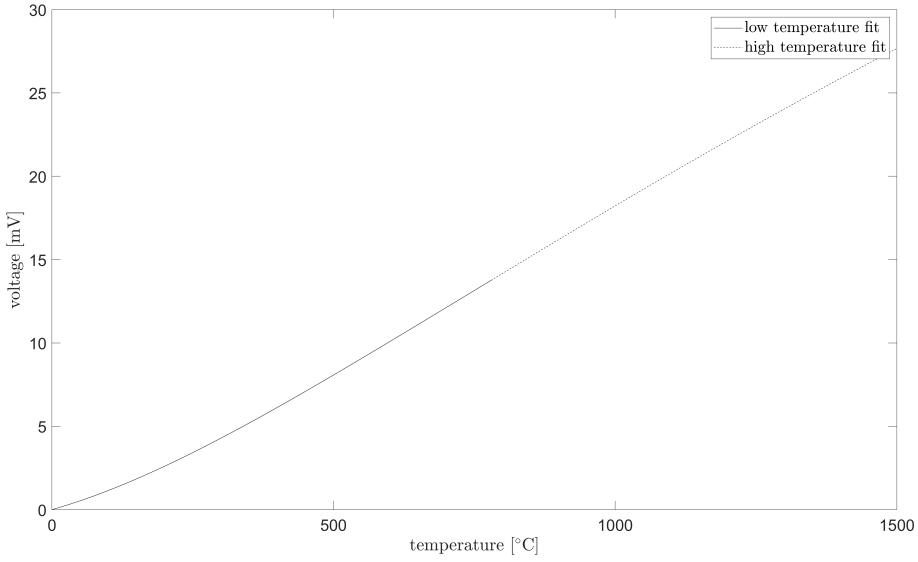

Figure 15: Combination of a low and high temperature fit for a WRe 3/25 (type D) thermocouple received from earlier measurements.

$$V = \sum_{n=0}^{5} a_n T_n \ , \tag{17}$$

with V the potential difference in mV and T the temperature difference in °C. The coef-

ficients a_n are shown below in table 2 and are different for the low and high temperature case. The transition from the low to high temperature case is at 780 °C. Due to the calibration of the thermocouple room temperature (20 °C) have to be added to the measured temperature.

Table 2: Coefficients a_n for the low and high temperature fit for a WRe 3/25 (type D) thermocouple.

	low T	**high T**
a_0	0	0
a_1	$9.5685256 \cdot 10^{-3}$	$9.9109462 \cdot 10^{-3}$
a_2	$2.0592621 \cdot 10^{-5}$	$1.8666488 \cdot 10^{-5}$
a_3	$-1.8464576 \cdot 10^{-8}$	$-1.4935266 \cdot 10^{-8}$
a_4	$7.9498033 \cdot 10^{-12}$	$5.3743821 \cdot 10^{-12}$
a_5	$1.4240735 \cdot 10^{-15}$	$-7.9026726 \cdot 10^{-16}$

To find the current which corresponds to a certain temperature the oven was heated with a constant current and after a long time the equilibrium temperature was measured. A smoothing spline fit was made through these data points and is shown in figure 16.

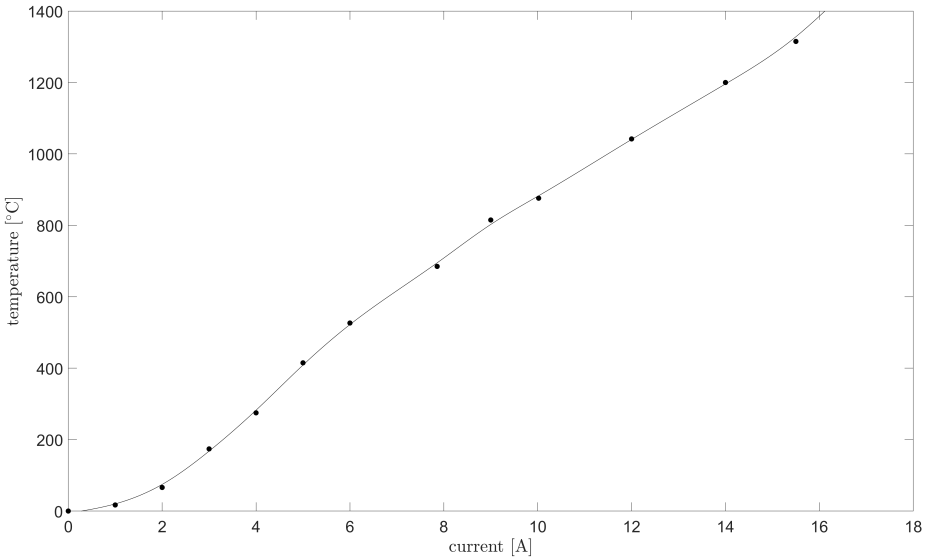

Figure 16: Oven current-temperature calibration curve. The marked points are the measured data, while the line is a smoothing spline fit.

To reach the desired temperatures quickly, first a higher than needed current was used. When the measured temperature approached the desired one, the current was decreased to the value corresponding to the desired temperature. In figure 17 an example of an annealing stage is shown with an average annealing temperature of 423 °C. In this example first a current of 8 A was used for 18 minutes followed by a current of 5 A to reach equilibrium. All other annealing stages can be found in appendix A.

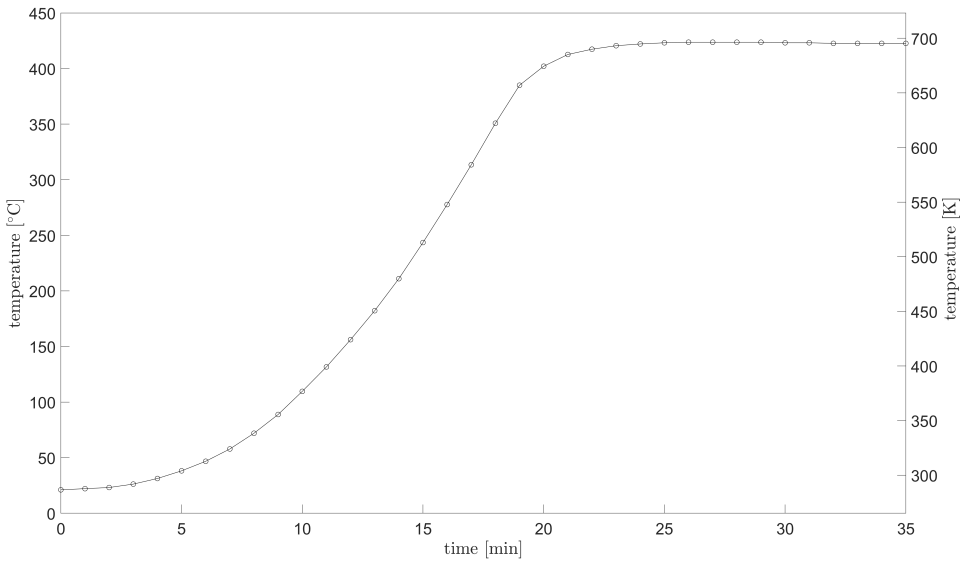

Figure 17: The third annealing stage of the VEP sample at a mean 423 °C for 10 minutes.

The samples were all annealed for 10 minutes at multiple constant temperature. The sample for the VEP measurements was annealed from 200 °C up to 1300 °C in steps of 100 °C. The lifetime samples were annealed from 200 °C up to 700 °C in steps of 100 °C and the hardness sample from 200 °C up to 1200 °C in steps of 200 °C. For clarity, all the annealing steps are summarised in table 3 per sample.

Table 3: Summary of the annealed temperatures for all measurements per sample and the aimed steps of 100 °C.

	VEP	**hardness**	**lifetime**
as received	as received	as received	as received
200 °C	187 °C	187 °C	191 °C
300 °C	312 °C		314 °C
400 °C	423 °C	426 °C	424 °C
500 °C	518 °C		521 °C
600 °C	620 °C	621 °C	620 °C
700 °C	721 °C		713 °C
800 °C	816 °C	815 °C	
900 °C	928 °C		
1000 °C	1031 °C	1031 °C	
1100 °C	1130 °C		
1200 °C	1199 °C	1201 °C	
1300 °C	1302 °C		

3.3 Positron annihilation Doppler broadening spectroscopy

The Doppler broadening spectroscopy measurements were performed in the Variable Energy Positron beam (VEP) at the Reactor Institute Delft (RID). This measurement set-up was built by Dr. H. Schut and it is in operation since 1988 [9]. The VEP creates a positron beam of circa 10^5 positrons per second with a variable energy and a diameter of approximately 8 mm. The photons emitted after annihilation are detected by a high purity Ge solid-state detector which has a resolution of 1.8 keV at 1.33 MeV. The data obtained was analysed using the software VEPFIT.

3.3.1 Positron source

The used positrons in the VEP are originating from a ^{22}Na source of 1 GBq. ^{22}Na is used because it fulfils best the requirements for positron annihilation spectroscopy from all known sources. These requirements include a high relative positron yield compared to the total activity, a practical half lifetime, no high energy gamma emission and a stable chemical composition.

^{22}Na can decay in multiple ways which are drawn schematically in figure 18. The emission of a positron and a 1274 keV photon is the most probable decay. The 1274 keV photon is used in lifetime measurements as explained in section 3.5.1.

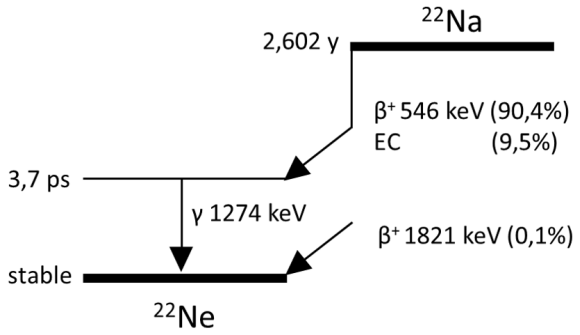

Figure 18: Schematic representation of the decay of ^{22}Na.

3.3.2 Measurement set-up

The positron beam is guided from the ^{22}Na source to the sample using electromagnetic coils. During this trajectory the positrons are also accelerated. This all takes place inside a vacuum of approximately 10^{-8} mbar. In figure 19 a schematic representation from the complete VEP set-up is shown. The five marked sections are separately discussed below.

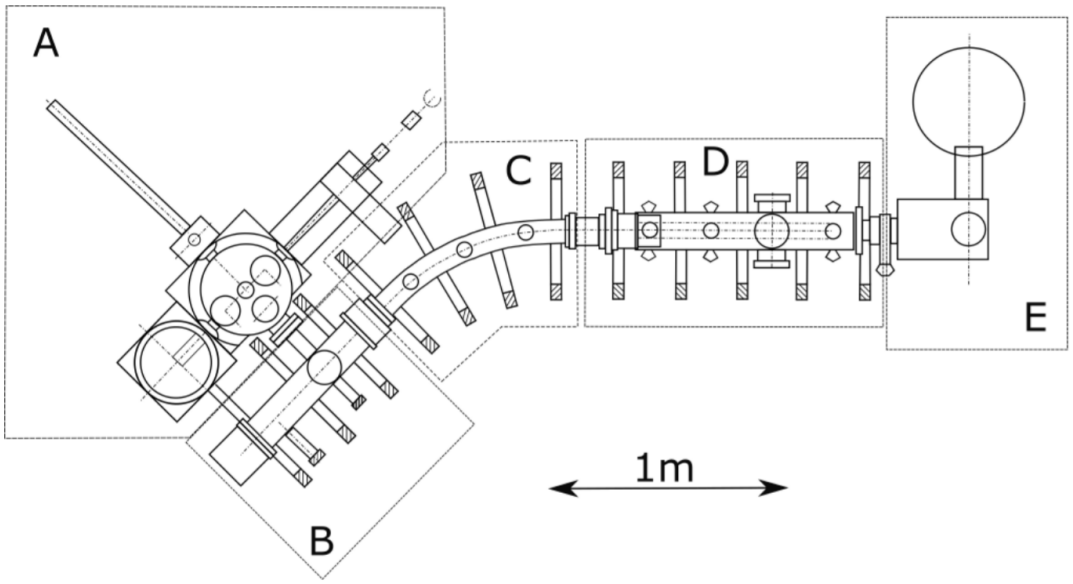

Figure 19: A schematic representation of the VEP measurement set-up. The set-up is divided in five different parts: with A and B the ^{22}Na source, C a filter to remove fast positrons, D the accelerator and E the measurement chamber. This image is retrieved from [7].

In section A the ^{22}Na sources are located inside a lead container, which safely stores old and unused sources. Besides the container there is also a transport system to move sources from the storage container in A to the source position in section B. The source located at this position is actually used for measurements. The positrons emitted from this source have a maximum energy of 546 keV as shown in figure 18. To control the energy of the positron beam a tungsten foil is located right next to the source, which reduces the energy of the positrons. Finally, the positrons are accelerated to 115 eV inside are B.

In area C the positrons with the wanted energy are filtered with the use of the Lorentz force. Beside filtering the coils creating a magnetic field in C, can also be used to focus the beam correctly on the sample. After this curve the positrons are accelerated to a desired energy using potential differences in area D. The VEP is limited to a maximum positron energy of 25 keV.

The last section of the VEP is the sample chamber E. The positrons are entering this chamber through a 10 mm diameter diaphragm and subsequently hit the sample to annihilate. The samples are fixed in a sample holder between thin stainless steel wires as shown in figure 20. During the annihilation two photons are emitted and detected by the high-purity germanium detector. Due to the photons creating electron-hole pairs, this detector delivers charge pulses which are converted into an electric signal. To limit thermal noise the detector is cooled with liquid nitrogen. Still, the signal to noise ratio of this signal is small and therefore the signal is amplified. Next, the analogue signal is converted by a ADC into a binary number. Finally, the signal is stored with the use of a multi-channel analyser (MCA). In figure 21 the detector set-up is shown schematically.

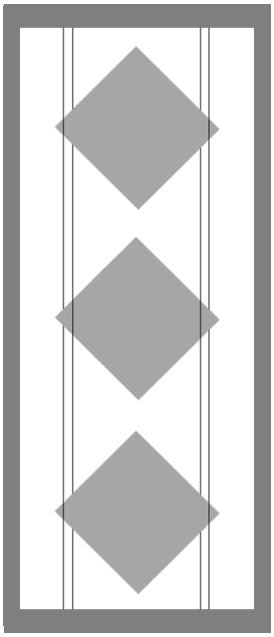

Figure 20: A sketch of the VEP sample holder.

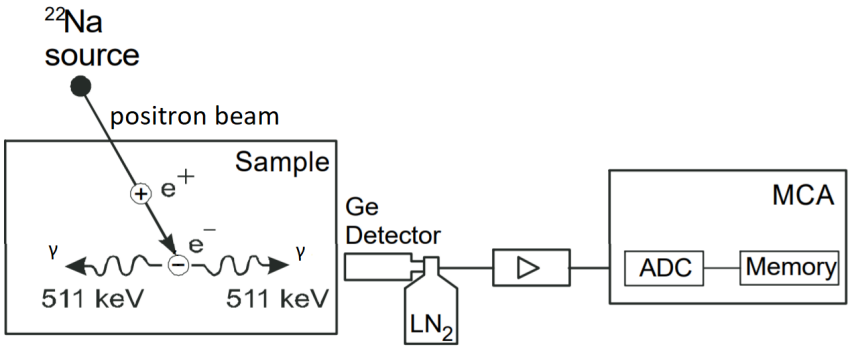

Figure 21: A schematic representation of the detector set-up of the VEP. This image is modified from [6].

From the data stored in the MCA the S and W parameter can be determined with the use of equations 5 and 6. Here the convention is used that the S parameter equals approximately 0.5, as explained in paragraph 2.2. The chosen boundaries are kept constant for all measurements to make them comparable. Also the areas A_S and A_W have to be chosen without overlap. The absolute errors of the S and W parameter are:

$$u(S) = \sqrt{\frac{S(1-S)}{A_0}} \approx \frac{S}{A_0}\,, \tag{18}$$

and

$$u(W) = \sqrt{\frac{W(1-W)}{A_0}}\,, \tag{19}$$

with A_0 the total area (counts) below the curve. The approximation in the S parameter can be made, because the S parameter is near 0.5 thus $S(1-S) \approx S^2$.

3.3.3 VEPFIT

To analyse the measured data VEPFIT is used. This software fits a curve through the measured S and W parameter versus the implantation energy with the use of the diffusion equation for positrons in matter (equation 11). In the samples no electric field is present, therefore, the term $\frac{d}{dz}(v_d c)$ equals zero in equation 11. Solving this equation leads to a positron concentration

$$c(z) = c(z_f)e^{-a(z-z_f)/L_+}\,, \tag{20}$$

with $c(z)$ the concentration at position z, a a dimensionless depth parameter (e.g. the lattice constant) and $L_+ = \sqrt{D^+/\lambda_b}$ the diffusion length in the pure material. In this derivation a boundary z_f is defined, which is the depth beyond which no positrons are stopped and no defects are present [20].

In this research model 5 was used to make a fit through the data points, which can fit layered structures of different materials. Because the studied material was homogeneous only one layer is used. The iron density (7.87 g/cm^3) is used, because this is a good approximation of the density of the sample.

VEPFIT quantises the implantation depth and determines a S and W value for each depth interval. To calculate the total S value depending on the implantation energy E, a

weighted sum over the individual S values is taken [20]:

$$S(E) = \sum_{i=1}^{N} S_i T_i + S_{surf} T_{surf} \ , \tag{21}$$

with N the total number of intervals, S_i the S value in depth interval i, T_i the fraction of positrons annihilating in interval i, S_{surf} the surface S value and T_{surf} the fraction of positrons returning to the surface. For the total W value the same equation is used but $S(E)$, S_i and S_{surf} are swapped for $W(E)$, W_i and W_{surf}, respectively.

3.4 Vickers hardness

The Vickers hardness measurements were performed with the use of the Struers Durascan, with a load of 0.3 kgf. For each annealing stage seven measurements were taken and an average value was determined.

The hardness measurement set-up is composed of an indenter, a microscope and a computer. The square-base pyramid diamond indenter is used to apply a constant load of 0.3 kgf on the sample. The light microscope is attached to the system, in order to allow the magnification of the view of the indentation made and to measure the diagonals of the indentation with included software. In figure 22 the four steps of the measurements are shown. In step 1 the indenter is above the sample and a location is chosen. Next, the indenter is pressed into the sample (step 2) and leaves an indentation as shown in the third step. Finally, the view of the indentation is enlarged with the use of a microscope and in the software four lines are set exactly at the edges of the corners (step 4). With this lines the software can calculate the diameters and convert that into a hardness value.

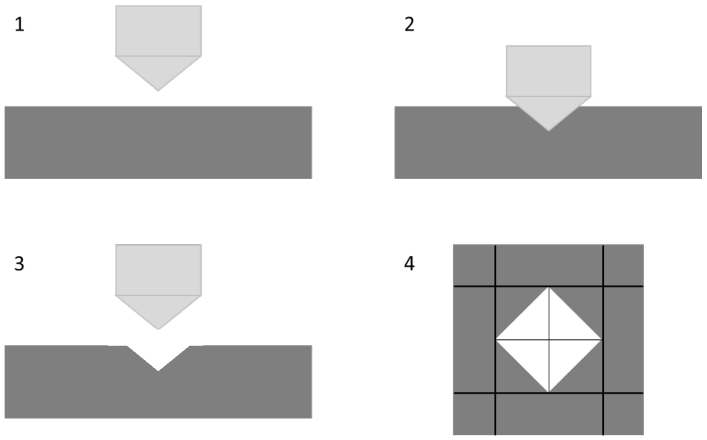

Figure 22: Schematic representation of the steps done in hardness measurements. In step 1 a location is chosen. In the second and third step the indentation is made and in the final step the diagonal are measured with the use of a light microscope.

In figure 23 a real image of the indentation is presented at a magnification of 1000x. In the bottom left the lengths of the diagonals are shown. The average of those is converted into a hardness value as follows:

$$HV = \frac{2P \sin(\frac{\theta}{2})}{d^2} = \frac{1854.4P}{d^2} \ , \tag{22}$$

with HV the hardness value, P the load in gf, θ the top angle of the pyramid (typically $\theta = 136°$) and d the average of the two diagonals in μm. This results in a hardness of 393 HV for this example.

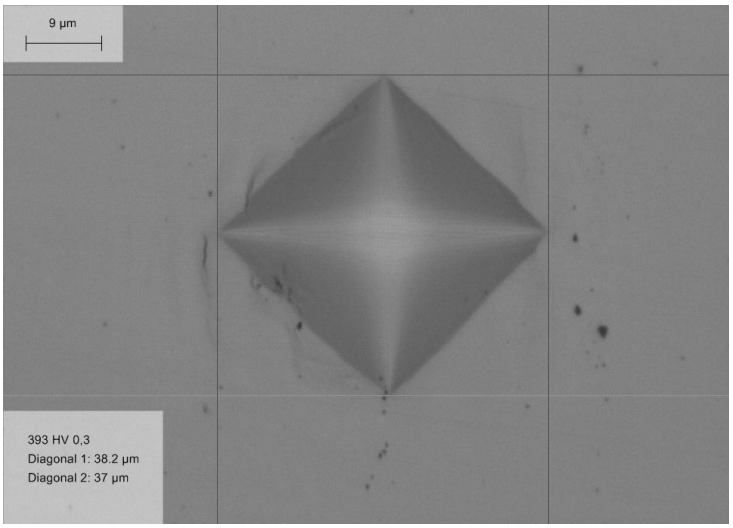

Figure 23: One of the seven measurements of the hardness sample after annealing at 621 °C.

After annealing the samples were checked with a light microscope to see whether the surface was still flat and shiny, because otherwise the diagonals of the hardness measurements could not be measured accurately. When the sample was not ready for measurement the sample was again metallographically prepared like discussed earlier (mounting, grinding and mechanically polishing).

3.5 Positron annihilation lifetime

To characterize the defects present in the steel, positron lifetime measurements were performed.

3.5.1 Measurement set-up

The lifetime measurement set-up is schematically shown in figure 24. In the middle a small ^{22}Na source is placed in between two thin kapton sheets of 7 μm thickness. This to prevent direct contact of the ^{22}Na with the samples. The two samples for lifetime are both carefully pressed against the kapton by an elastic surface inside a plastic container. At both sides of this container a scintillator and a photomultiplier are placed to measure the photons emitted. Two different types of photons are emitted in this process. As discussed in section 3.3.1 the ^{22}Na source itself emits a 1274 keV photon together with the positron. The ^{22}Na emitted photon has a half lifetime of 3.7 ps. Hence, this photon marks the birth of a positron. On the other hand, the well known 511 keV are originating from the annihilation process of positrons. Therefore the lifetime of positrons can be determined by measuring the time difference at which these photons are detected. This is done with the two scintillators and photomultipliers. One of them is adjusted to only detect 1274 keV photons and the other, to detect 511 keV photons. When a 1274 keV photon is detected a electric "stopwatch" is started and when the 511 keV photon is detected the watch is stopped. These signals are stored in a multi-channel analyser (MCA). To make a full lifetime spectrum at least one million counts are necessary [6].

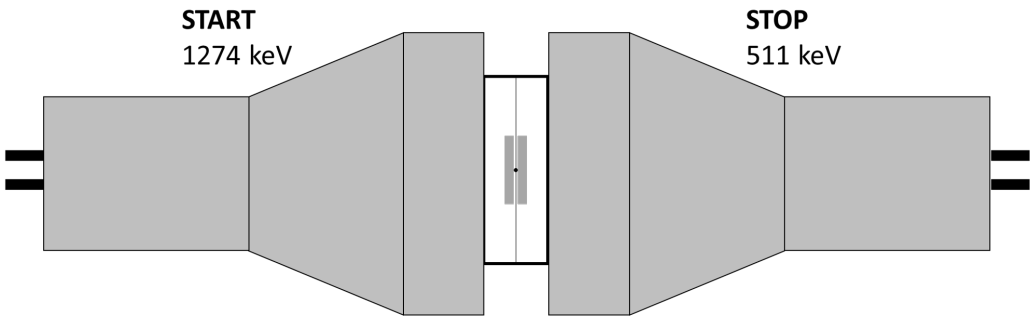

Figure 24: The lifetime measurement set-up shown schematically. In the middle the ^{22}Na source in kapton with two samples pressed against it. On the left the 'start' scintillator-photomultiplier which detects 1274 keV photons and on the right the 'stop' one for 511 keV photons.

3.5.2 Fitting

When enough counts are received the data can be fitted and an average lifetime of the sample can be determined. In figure 25 an example of a measured lifetime spectrum is shown. The dots are the measured counts per time difference. Note that there are negative time differences due to the convolution of exponential function of the lifetime and two Gaussians of the resolution.

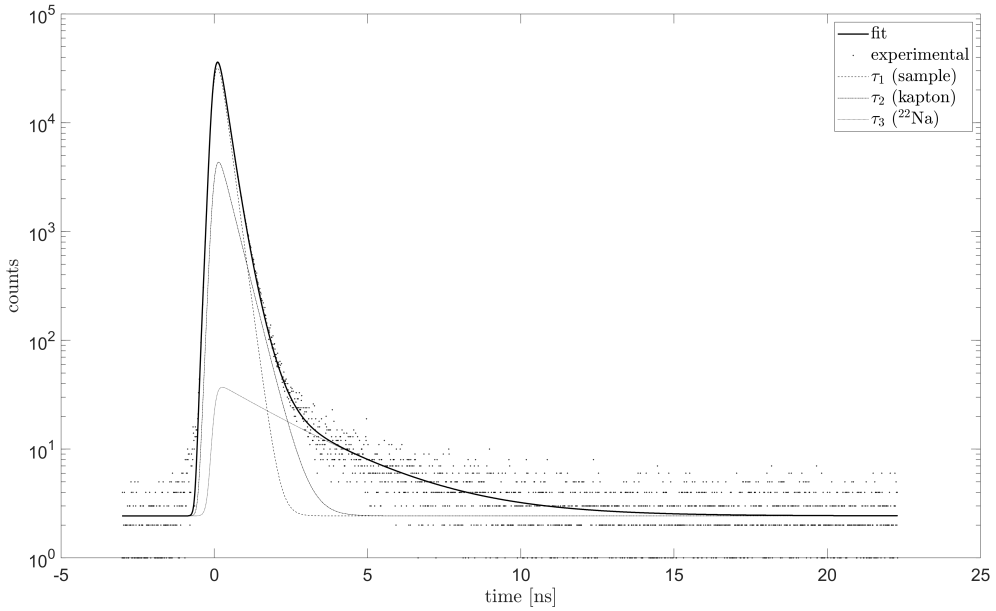

Figure 25: The measured lifetime spectrum after annealing at 424 °C of ODS 12Cr steel. The dots are the measured counts, while the solid line is a fit through the data points. The other three lines are the fitted lifetimes, where τ_1 is the average lifetime of the sample and the other two are the lifetimes of the source.

The used fitted program is LT 9.2. All lifetime measurements were fitted at the same time with some variables fixed, some fitted and some global fitted (fitted but the same for each measurement). The lifetime of the kapton is well known and therefore fixed. Also the fraction of the second ESG is fixed. The contribution of the source to the lifetime, the intensity of the first and second lifetime of the source and the lifetime of the sodium on the other hand are globally fitted since they are expected to be the same for all measurements. The other parameter such as the average lifetime of the sample and the background are fitted for every different data set. In figure 25 the fitted lifetime of the sample τ_1 and respectively the lifetimes of the kapton and ^{22}Na τ_2 τ_3 are shown.

Chapter 4

Results

The results of the different measurements are presented in this chapter. First the effect of electrolytically polishing on the bulk values of the S and W parameter are shown in paragraph 4.1. Subsequently, the different results of the Doppler broadening spectroscopy, hardness and lifetime measurements are given in the paragraphs 4.2, 4.3 and 4.4, respectively. The temperature behaviour during the annealing stages of the different samples are shown in appendix A.

4.1 Effect of electrolytically polishing

In figure 26 the S value at different implantation energies is shown for the two differently prepared samples. The filled circles are the measurements of the only mechanically polished sample while the open circles are the both mechanically and electrolytically polished sample. The crosses are the results after only grinding one of the samples. The lines are the VEPFIT results.

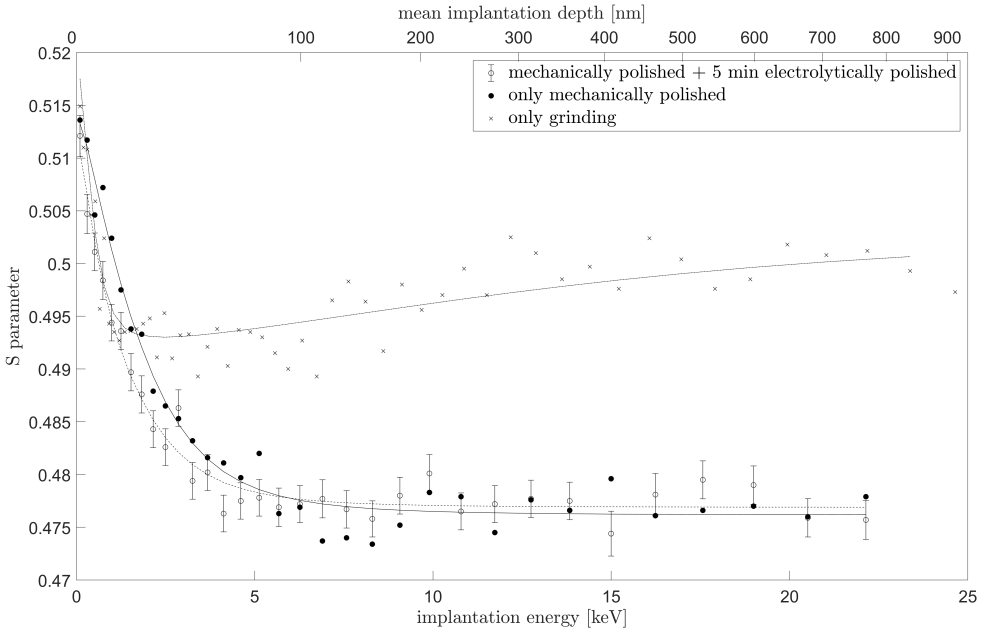

Figure 26: The S parameter at different implantation energies for the only mechanically polished (filled circles) and the both mechanically and electrolytically polished (open circles) sample in the as received condition. The crosses are measurements after only grinding the sample. The solid line is the VEPFIT result of the filled circles, while the dashed line is the one for the open circles. The errors are for all measurements approximately the same, but for clarity only one is plotted with error bars.

Also the W parameter has been determined for different implantation energies for these two samples. These results can be seen in figure 27.

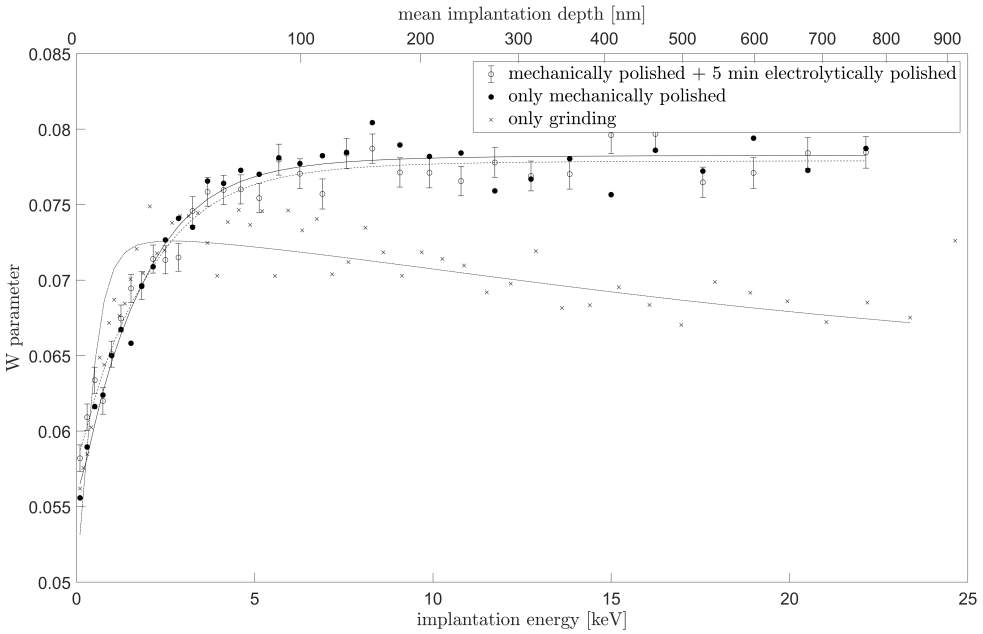

Figure 27: The W parameter at different implantation energies for the only mechanically polished (filled circles) and the both mechanically and electrolytically polished (open circles) sample in the as received condition. The crosses are measurements after only grinding the sample. The solid line is the VEPFIT result of the filled circles, while the dashed line is the one for the open circles. The errors are for all measurements approximately the same, but for clarity only one is plotted with error bars.

Note that the bulk S and W parameter are approximately the same for the different polishing methods, because their difference is smaller than one standard deviation. It shows that mechanically polishing with 0.04 μm alumina particles removes completely the deformed layer introduced in the previous polishing steps. Therefore, the lifetime measurements have been done with these two samples without further preparation. On the other hand, the result of grinding is completely different and shows that polishing is needed before positron annihilation measurements.

4.2 Positron annihilation Doppler broadening spectroscopy

The S and W parameter were measured after each annealing stage up to 1300 °C in steps of 100 °C. The development of the S parameter throughout the annealing stages is shown in figure 28. In this figure the S parameter is plotted against the implantation energy after each annealing stage. The lines are the result of the VEPFIT analysis. Figure 29 shows the W parameter.

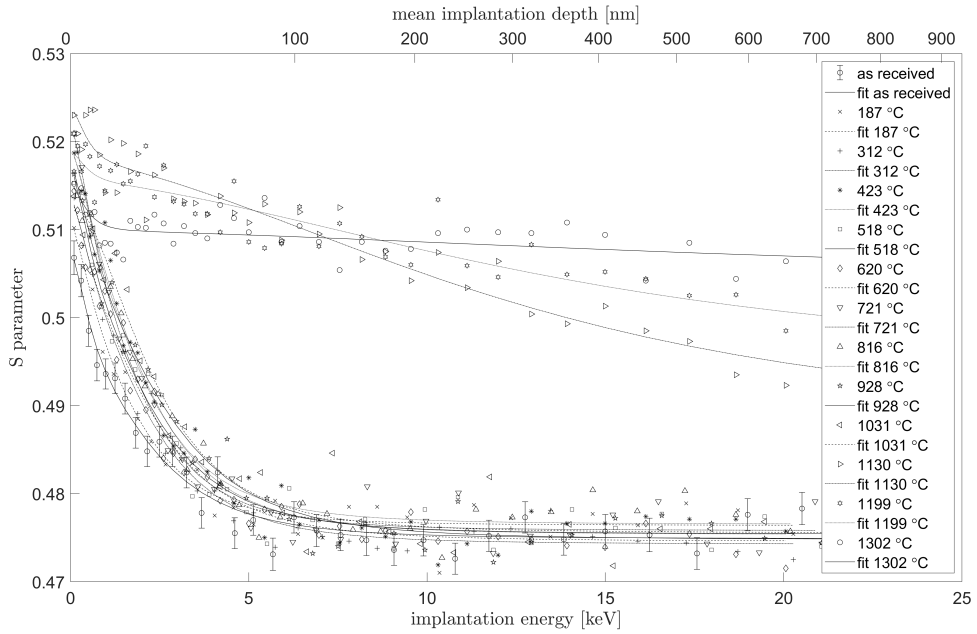

Figure 28: The S parameter plotted against the implantation energy after all annealing stages.

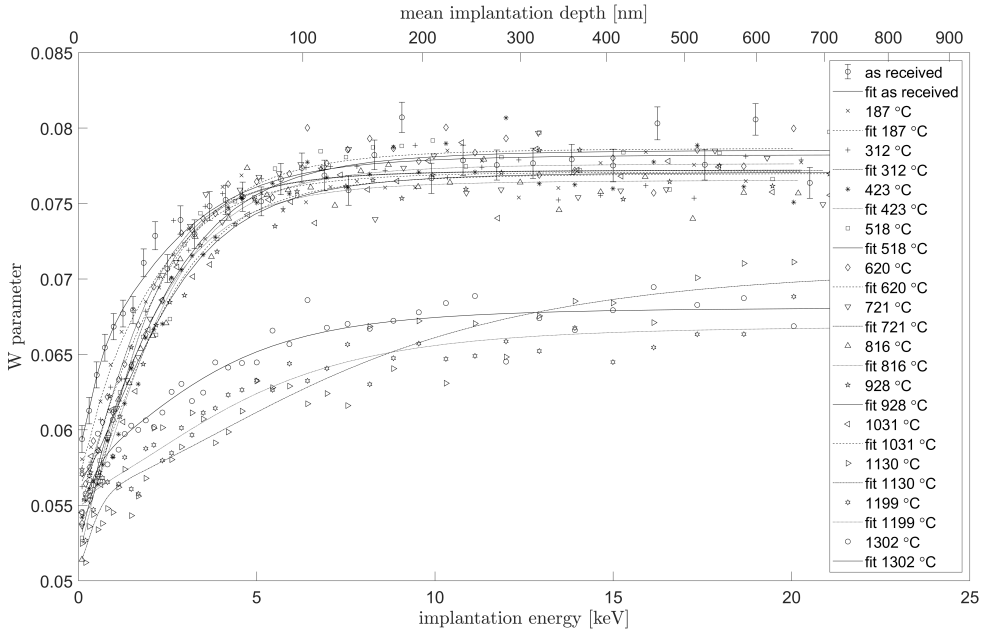

Figure 29: The W parameter plotted against the implantation energy after all annealing stages.

Two trends can be recognised in figures 28 and 29. The S and W parameters stay approximately constant after annealing up to 1100 °C and vary above this temperature. The first trend contains the annealing stages up to 1031 °C and the second trend the annealing stages from 1130 °C and up. In the second trend the bulk S parameter increases with increasing annealing temperatures and the bulk W parameter decreases. In appendix B the S and W parameters are plotted against the implantation energy for each annealing stage separately.

All the S and W parameter show a constant bulk value for implantation energies higher then 10 keV. Those bulk values are found with VEPFIT and are given in table 4. In figures 30 and 31 they are also plotted versus the annealing temperature.

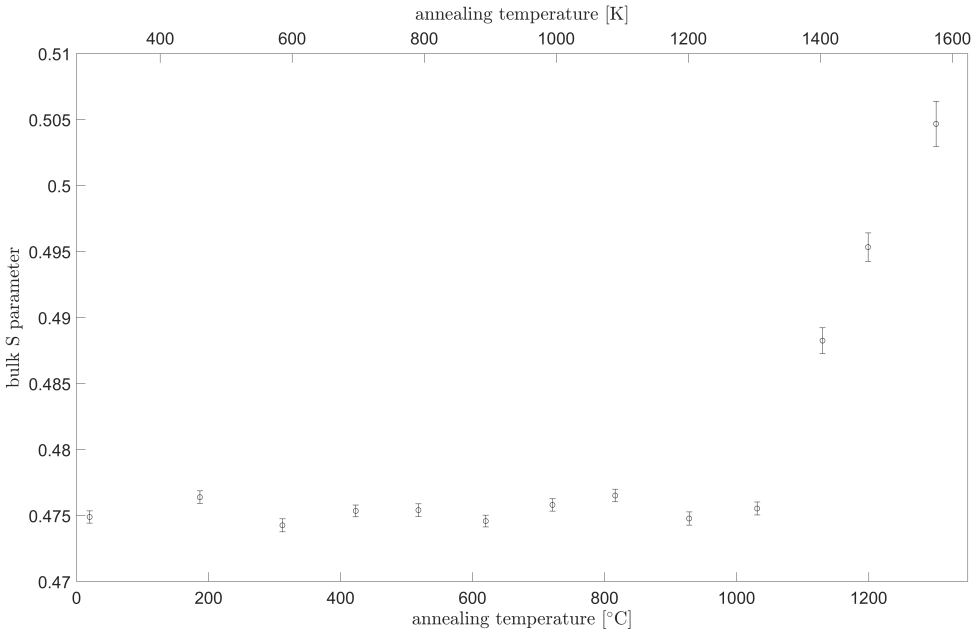

Figure 30: The bulk S parameter plotted against the implantation energy and the mean implantation depth after annealing for 10 minutes at different temperatures.

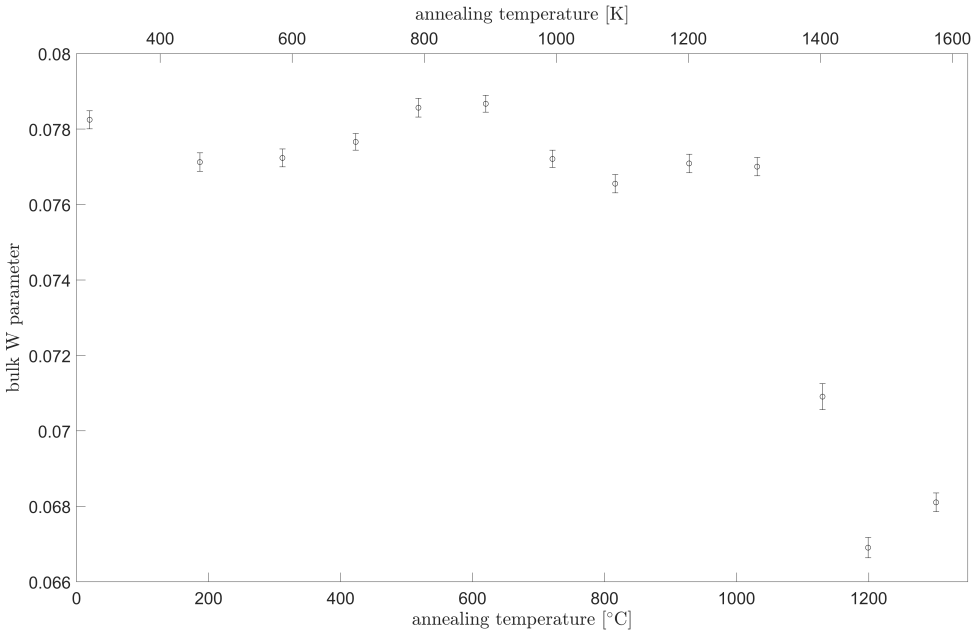

Figure 31: The bulk W parameter plotted against the implantation energy and the mean implantation depth after annealing for 10 minutes at different temperatures.

Table 4: S and W parameters of ODS 12Cr steel after annealing for ten minutes at different temperatures found with VEPFIT. The uncertainty in the last decimal is shown in the brackets.

annealing temperature [°C]	**bulk S parameter**	**bulk W parameter**
as received	0.4749(5)	0.0782(2)
187	0.4764(5)	0.0771(2)
312	0.4743(5)	0.0772(2)
423	0.4753(4)	0.0777(2)
518	0.4754(5)	0.0786(2)
620	0.4746(5)	0.0787(2)
721	0.4758(5)	0.0772(2)
816	0.4765(5)	0.0766(2)
928	0.4748(5)	0.0771(2)
1031	0.4755(5)	0.0770(2)
1130	0.4882(10)	0.0709(3)
1199	0.4953(11)	0.0669(3)
1302	0.5047(17)	0.0681(2)

Besides the bulk values, the diffusion length is a way to compare the curves shown in figure 28 and 29. It is a measure for the annihilation of trapped positrons in defects. The diffusion lengths are also retrieved from VEPFIT. The diffusion length is plotted in figure 32 against the annealing temperature for both the fits of the S and W parameter.

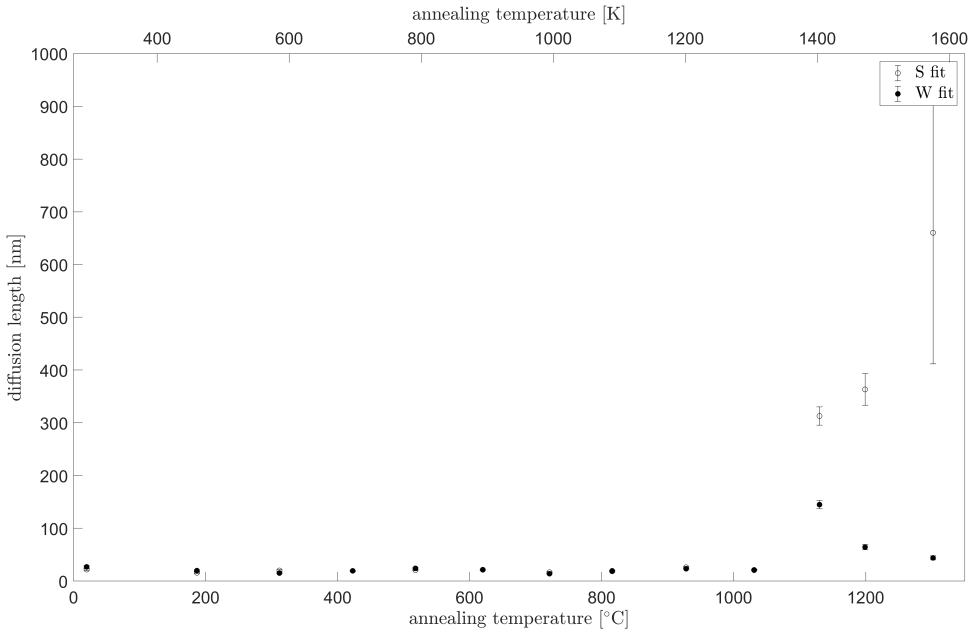

Figure 32: The fitted diffusion lengths for the S and W fits are plotted against the annealing temperature.

Note that the diffusion length is constant (± 20 nm) in the earlier called first trend and for S and W approximately the same as necessary. The diffusion length in defect free iron is around 100 nm and the diffusion length decreases with defects being present. Therefore, the diffusion length in the second trend are non realistic and the model used in VEPFIT was not suitable for these results.

Finally, the bulk S and W parameters can be plotted against each other for the different annealing temperatures. This is called a SW map and is plotted in figure 33. Again it can be seen that the S and W parameters are approximately constant until annealing temperatures of 1031 °C. The values vary strong in the second trend. The open circles in figure 33 show earlier measurements with ODS Eurofer which is an iron based alloy with approximately 9 weight percentage chromium. Note that the S values of the ODS 12Cr steel at temperatures above 1100 °C are significantly higher than for ODS Eurofer. The ODS Eurofer shows a decrease in S and increase in W until a turning point between 920 °C and 1120 °C, after which the S increases and W decreases. This behaviour is not seen for the ODS 12Cr steel. Also, the ODS Eurofer data lays approximately on one straight line with higher W and lower S bulk values than a line through the ODS 12Cr steel data
.

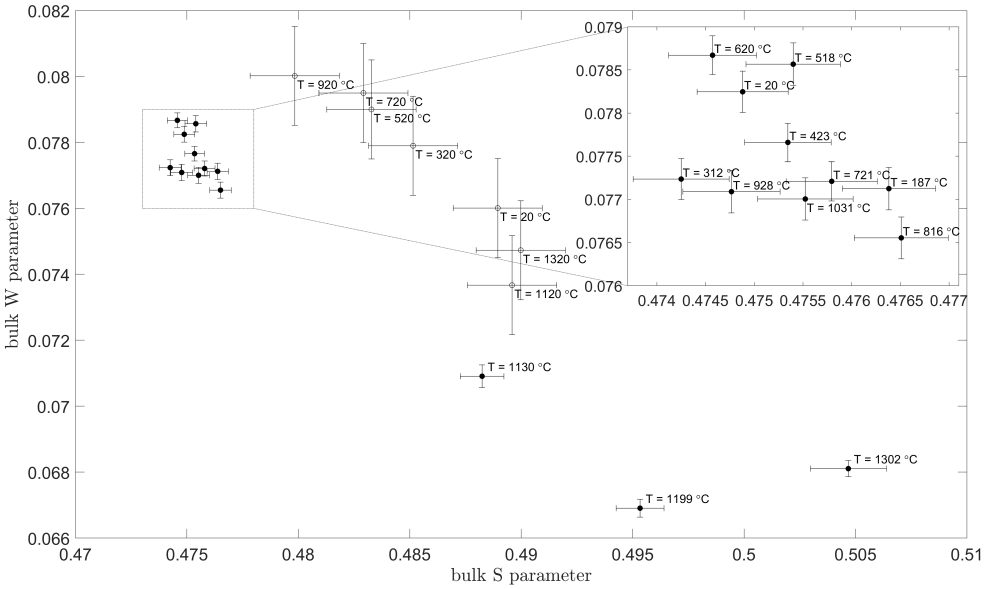

Figure 33: SW map for the ODS 12Cr steel (filled circles) and ODS Eurofer (open circles). The bulk SW points are marked with their annealing temperatures.

4.3 Vickers hardness

In table 5 and figure 34 the average Vickers hardness of the seven measurements are shown per annealing temperature. Note that the values up to 1031 °C are approximately constant at a hardness value of 395 HV and comparable with earlier measurements. The horizontal line in figure 34 represents the weighted average (395 HV) of the measurements up to 1031°C. The hardness decreases significantly after annealing at 1201 °C.

Table 5: Average of the seven Vickers hardness measurements and the standard deviations of ODS 12Cr steel after annealing for ten minutes at different temperatures.

annealing temperature [°C]	**average Vickers hardness [HV]**	**standard deviation**
as received	395.7	21.0
187	393.4	15.7
426	389.7	8.6
621	391.6	12.8
815	400.1	7.1
1031	395.0	10.4
1201	374.0	7.2

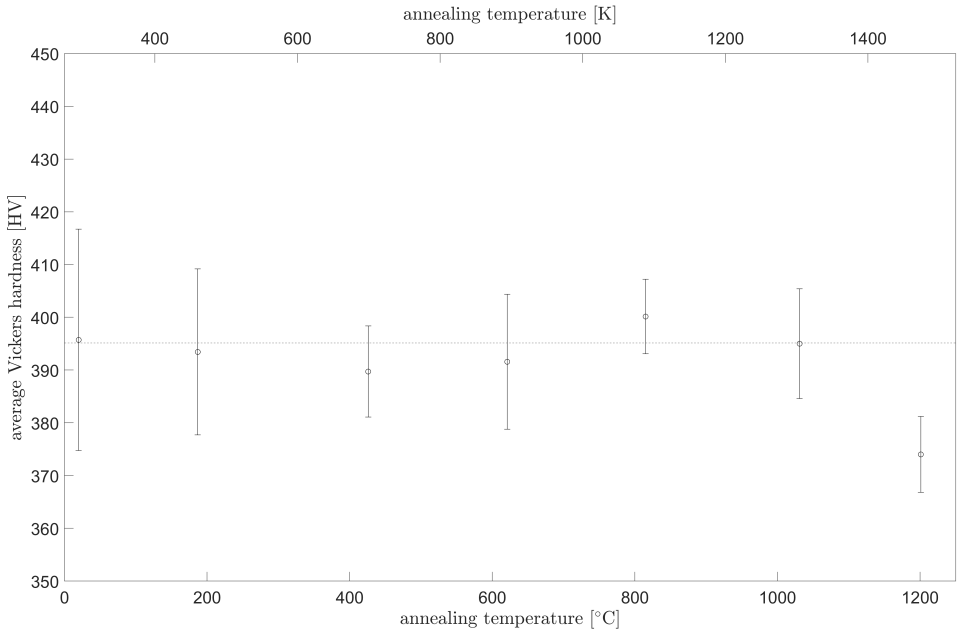

Figure 34: The average Vickers hardness of ODS 12Cr steel after annealing for ten minutes at different temperatures. The horizontal lines is located at 395 and is a weighted average of the measurements up to 1031 °C.

4.4 Positron annihilation lifetime

The fitted average lifetime of ODS 12Cr steel is given in table 6 for different annealing temperatures. These lifetimes are also plotted in figure 35. In this figure also the calculated lifetimes for different types of defects present in pure iron are marked [21][22]. Note that the lifetime of the positrons stay constant at approximately 208 ps (continuous horizontal line in figure 35), which corresponds with defects with sizes comparable to or at least larger than that of divacancies.

Table 6: Fitted average lifetime of ODS 12Cr steel after annealing for ten minutes at different temperatures. All lifetimes have an error of approximately 3 ps.

annealing temperature [°C]	**average lifetime [ps]**
as received	203
191	208
314	210
424	205
521	212
620	202
713	209

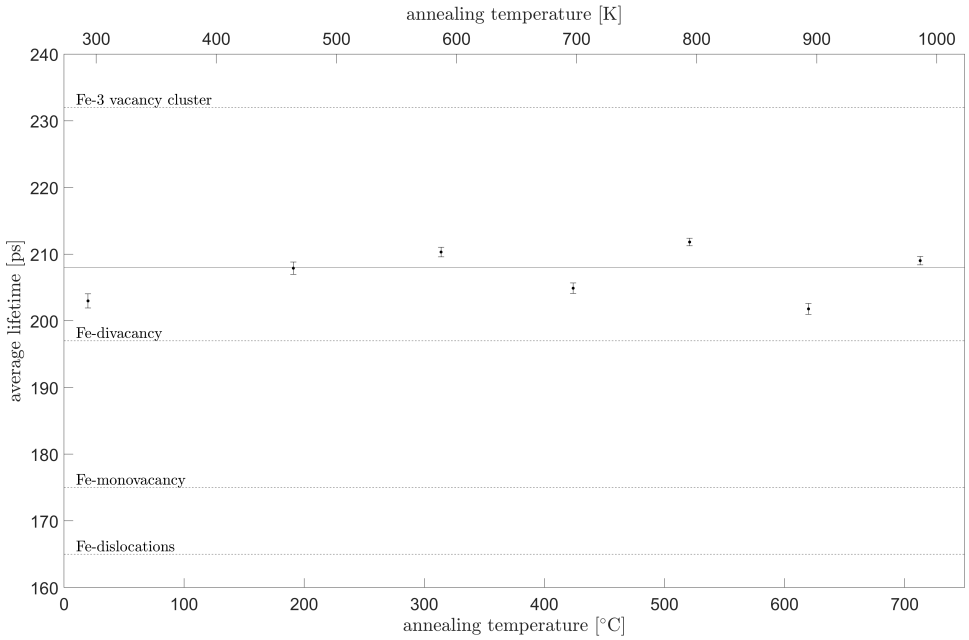

Figure 35: Average lifetime plotted versus the annealing temperature. The dashed horizontal lines represent calculated lifetimes for different type of defects present in pure iron [21][22]. The continuous horizontal line represents the average of 208 ps.

Chapter 5

Discussion

In all the results two trends can be seen: the first one up to annealing temperatures of 1000 °C and the second one between 1100 °C and 1300 °C. In this chapter both trends will be discussed and explained separately.

The first trend shows no significant change in the S and W parameter, the hardness value and the lifetime. Therefore, it can be concluded that the defect concentration stays constant in this temperature domain. This behaviour is expected since no phase transformations happen at these temperatures as shown in figure 10 and 11. Besides the constant phase, the concentration of thermal vacancies stays low in this temperature range, see paragraph 2.5. At these temperatures the defects do not have enough energy to liberate themselves from the oxide particles [14]. Consequently, the number and type of defects stay constant and no difference should be seen in the S and W parameter as well as the average lifetime. The hardness value is kept constant by the nano-oxide particles too. Besides trapping vacancies they also pin grains, not allowing them to grow and hence keeping the hardness constant.

After annealing between 1100 °C and 1300 °C, the S and W parameter behave differently. The S and W parameter show a much lower convergence near the surface which indicates a layer formation. An oxide layer can be formed during annealing at high temperatures, because temperature increases the oxidation rate. This is supported by the appearance of the sample. After these annealing stages the sample was significantly less shiny than before. Besides the lower convergence of the S and W parameter, the bulk values change significantly too. The increase in the S bulk parameter indicates that more defects are present than in the earlier measurements. A first guess could be the dissolution of titanium carbides at this temperatures having some effect on the bulk values. However, this can not be the case, because when carbides dissolve their interfaces with the matrix are removed and this would lead to a decrease in defect density and in the S value. The higher S parameter can on the other hand be caused by the rise of the thermal vacancy concentration for this temperatures, see paragraph 2.5. Besides the increase in thermal vacancies, the oxide particles become coarse because of their cluster forming. This coarsening creates large voids with some clustered oxide particles resulting in larger defects and therefore higher S parameters.

The second trend ($T > 1100$ °C) shows a change in hardness value too. It decreases from 395 HV at lower temperature to 374 HV at 1200 °C as shown in the results. This decrease in hardness can be explained by grain growth. At lower temperatures the oxide particles prevent the grains to grow by pinning them. But at higher temperatures above 1000 °C

the energy in the lattice structure increases which forces them to grow and decreases the hardness [24].

Compared with ODS Eurofer, an iron based alloy with 9 weight percentage chromium, the ODS 12Cr steel shows different behaviour. At temperatures up to 920 °C the S value of the ODS Eurofer decreases while the ODS 12Cr shows constant values up to 1031°C. At higher temperatures, both show a significant increase in S and a decrease in W, but the ODS 12Cr S values are 0.1 larger. The main difference between both steels is the chromium content, indicating that possibly chromium is the origin of the differences. Clustering of chromium atoms can result in open volume at grain boundaries which increases the S values. At lower temperatures the S and W bulk values stay constant, imposing the chromium being stable. This could origin from the last step of the possible production process, an annealing stage. When the annealing temperature during this research becomes larger than in the production process, the atoms gain more freedom than ever before, resulting in the formation of a new equilibrium condition. This could explain the sudden change in S and W around 1100 °C and the constant values before. A Doppler broadening measurement on pure chromium and locating it in the SW plot could be done to test this statement.

Possible improvements for this research could be taking equal step size for all the measurements. The VEP sample was annealed in a constant way with steps of 100 °C while the hardness one was annealing with steps of 200 °C. The effect of the different step sizes is unknown, however, the results are still corresponding. The lifetime sample on the other hand was annealed in the same way as the VEP, but was stopped earlier due to time limitation. Prospective studies therefore could be done by continuing the measurements with the lifetime sample and see whether the two trends were visible. Also more VEP and hardness measurements during the transition from the first to the second trend would be interesting. Further, TEM imaging of the samples after different annealing steps would be useful to really see nano-oxide particles and check there operation. This could support the given statements about their behaviour. Future EBSD measurements could prove the coarsening of oxide particles resulting in lower hardness values.

Chapter 6

Conclusion

In this research the behaviour of ODS 12Cr steel under thermal treatment has been studied at micro and macro level. At both levels the results show two trends: one up to 1000 °C and the other up from 1100 °C. In the lower trend all the measurements stayed constant. The bulk S and W parameter are respectively 0.475 and 0.078, while the Vickers hardness value is 395 HV and comparable with earlier measurements. The lifetime measurements resulted in an average lifetime of 208 ps, which corresponds with defects with sizes comparable to or at least larger than that of divacancies. The constant behaviour is explained by a low amount of thermal vacancies at these temperatures and the nano-oxide particle trapping the defects. Also, a production annealing temperature around 1100 °C could explain this behaviour. At higher temperatures an oxide layer is forming which changes the S and W parameter behaviour near the surface. The bulk values change also, due to the increase of thermal vacancies and the clustering of oxide particles. Comparing the S and W values with an iron alloy with less chromium, shows that the bulk S parameters of ODS 12Cr are large. This difference can originate from the cluster forming of chromium atoms resulting in more defects and a high S value. The hardness value also shows a decrease in operation of the oxide particles. It decreases significantly to 374 HV at 1200 °C due to grain growth. Concluding, the ODS 12Cr steel keeps its properties until 1000 °C and shows slightly decreasing properties at higher temperatures which make it a good candidate for future nuclear reactors.

Interesting follow-up research would be continuing the measurements with the lifetime sample to see whether a change happens after 1000 °C like with the other two measurements. TEM and EBSD imaging could visualise the nano-oxide particles and support the statements made. Doppler broadening measurements on chromium and comparing them in a SW plot with the result, could verify the clustering of chromium. In depth research with different measurement methods into the transition region between 1000 °C and 1100 °C would be interesting too.

Bibliography

[1] D.K. Mukhopadhyay, F.H. Froes, and D.S. Gelles. Development of oxide dispersion strengthened ferritic steels for fusion. *Journal of Nuclear Materials*, 258-263:1209–1215, October 1998.

[2] J. Ohta, T. Ohmura, K. Kako, M. Tokiwai, and T. Suzuki. Hardness of 12Cr8Mo ferritic steels irradiated by Ni ions. *Journal of Nuclear Materials*, 225:187–191, August 1995.

[3] L. Hsiung, M. Fluss, S. Tumey, J. Kuntz, B. El-Dasher, M. Wall, B. Choi, A. Kimura, F. Willaime, and Y. Serruys. HRTEM study of oxide nanoparticles in K3-ODS ferritic steel developed for radiation tolerance. *Journal of Nuclear Materials*, 409(2):72–79, February 2011.

[4] D. Häussler, M. Bartsch, U. Messerschmidt, and B. Reppich. HVTEM in situ observations of dislocation motion in the oxide dispersion strengthened superalloy MA 754. *Acta Materialia*, 49(18):3647–3657, October 2001.

[5] D.J. Griffiths. *Introduction to elementary particles; 2nd rev. version*. Physics textbook. Wiley, New York, NY, 2008.

[6] R. Krause-Rehberg and H.S. Leipner. *Positron Annihilation in Semiconductors: Defect Studies*, volume 127. Springer-Verlag Berlin Heidelberg, 1 edition, 1999.

[7] I. Monteiro De Sena Silvares De Carvalho. *Steels for nuclear reactors: Eurofer 97*. PhD thesis, 2016.

[8] M.J. Puska and R.M. Nieminen. Theory of positrons in solids and on solid surfaces. *Rev. Mod. Phys.*, 66:841–897, Jul 1994.

[9] H. Schut. *A variable energy positron beam facility with applications in materials science*. PhD thesis, 1990.

[10] I.Y. Dekhtyar. The use of positrons for the study of solids. *Physics Reports*, 9(5):243–353, March 1974.

[11] H. Kanazawa, Y.H. Ohtsuki, and S. Yanagawa. Positronium Formation in Metals. *Phys. Rev.*, 138:A1155–A1157, May 1965.

[12] S.G. Karshenboim. Precision study of positronium: testing bound state QED theory. *International Journal of Modern Physics A*, 19(23):3879–3896, September 2004.

[13] W.D. Callister. *Materials Science and Engineering: An Introduction*. Wiley, feb 2006.

[14] H. Matter, J. Winter, and W. Triftshäuser. Phase transformations and vacancy formation energies of transition metals by positron annihilation. *Applied Physics*, 20(2):135–140, October 1979.

[15] M. Laurent-Brocq, F. Legendre, M.H. Mathon, A. Mascaro, S. Poissonnet, B. Radiguet, P. Pareige, M. Loyer, and O. Leseigneur. Influence of ball-milling and annealing conditions on nanocluster characteristics in oxide dispersion strengthened steels. *Acta Materialia*, 60(20):7150–7159, December 2012.

[16] S. Ukai and M. Fujiwara. Perspective of ODS alloys application in nuclear environments. *Journal of Nuclear Materials*, 307-311:749–757, December 2002.

[17] E. Arzt and D.S. Wilkinson. Threshold stresses for dislocation climb over hard particles: The effect of an attractive interaction. *Acta Metallurgica*, 34(10):1893 – 1898, 1986.

[18] H. Springer, C. Baron, A. Szczepaniak, E.A. Jägle, M.B. Wilms, A. Weisheit, and D. Raabe. Efficient additive manufacturing production of oxide- and nitride-dispersion-strengthened materials through atmospheric reactions in liquid metal deposition. *Materials & Design*, 111:60–69, December 2016.

[19] T. Muroga, T. Nagasaka, Y. Li, H. Abe, S. Ukai, A. Kimura, and T. Okuda. Fabrication and characterization of reference 9cr and 12cr-ods low activation ferritic/martensitic steels. *Fusion Engineering and Design*, 89(7-8):1717–1722, 2014.

[20] A. van Veen, H. Schut, J. de Vries, R.A. Hakvoort, and M.R. IJpma. Analysis of positron profiling data by means of "VEPFIT". In *AIP Conference Proceedings*, volume 218(1), pages 171–198. AIP, 1991.

[21] P. Hautojärvi, L. Pöllänen, A. Vehanen, and J. Yli-Kauppila. Vacancies and carbon impurities in α-iron: neutron irradiation. *Journal of Nuclear Materials*, 114(2-3):250–259, 1983.

[22] A. Vehanen, P. Hautojärvi, J. Johansson, J. Yli-Kauppila, and P. Moser. Vacancies and carbon impurities in α-iron: electron irradiation. *Physical review B*, 25(2):762, 1982.

[23] T. Hayashi, P.M. Sarosi, J.H. Schneibel, and M.J. Mills. Creep response and deformation processes in nanocluster-strengthened ferritic steels. *Acta Materialia*, 56(7):1407–1416, April 2008.

[24] F. Mizana Shamsudin, S. Radiman, Y. Abdullah, and N. A. Hamid. The Effect of Annealing to the Hardness of High Y2O3-Oxide Dispersion Strengthened (ODS) Ferritic Steels. *Sains Malaysiana*, 47:189–193, 01 2018.

Appendices

Appendix A

Annealing stages

A.1 VEP sample

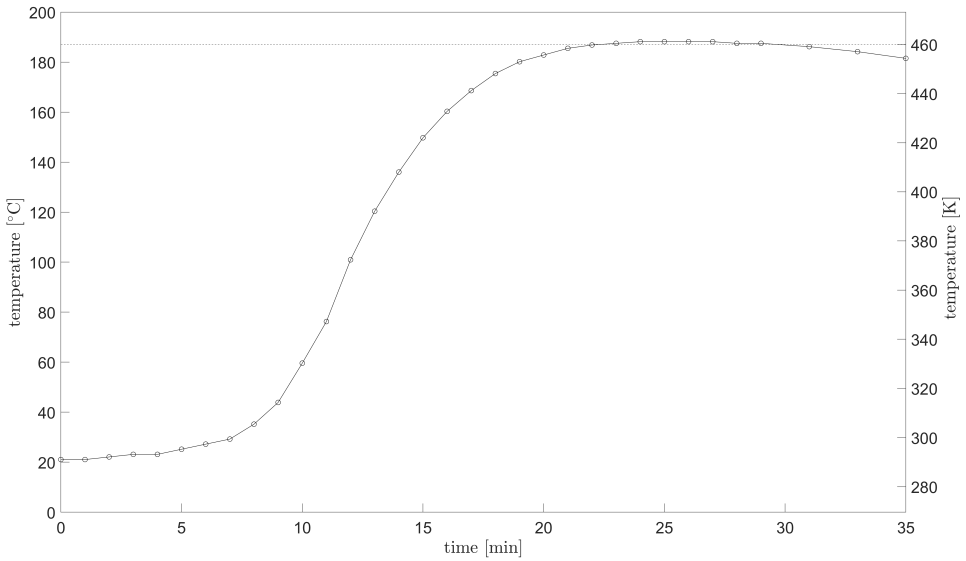

Figure 36: The first annealing stage of the VEP sample. The dotted line shows the mean annealing temperature of 187 °C for 10 minutes.

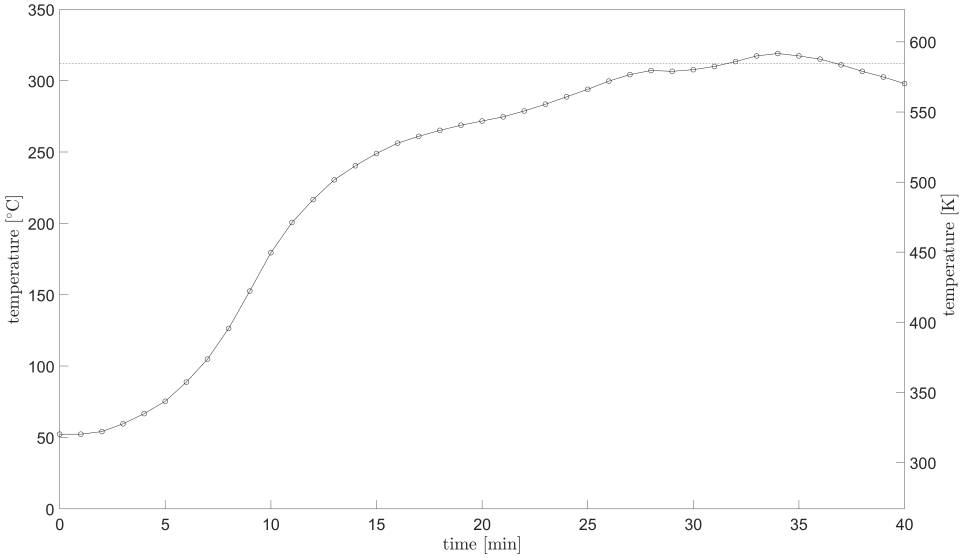

Figure 37: The second annealing stage of the VEP sample. The dotted line shows the mean annealing temperature of 312 °C for 10 minutes.

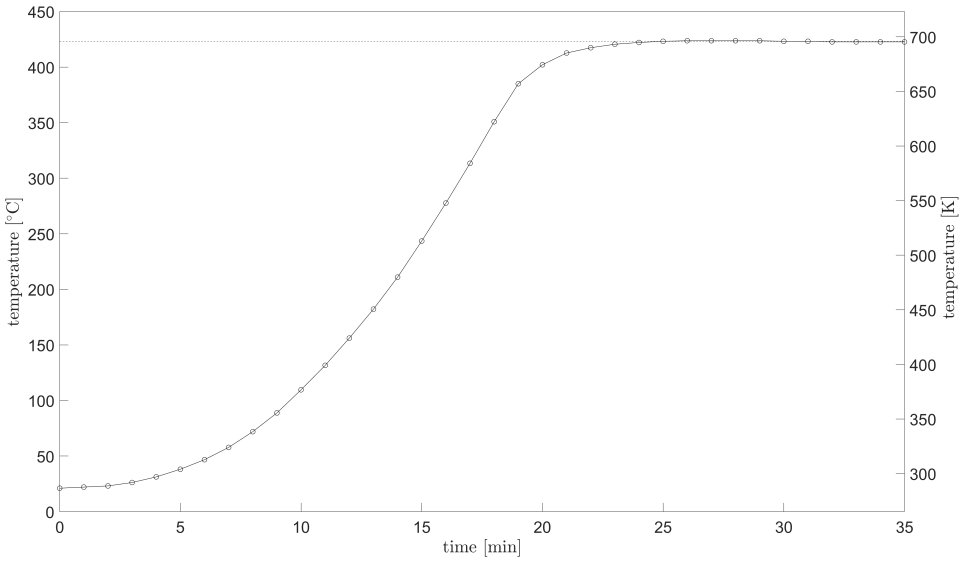

Figure 38: The third annealing stage of the VEP sample. The dotted line shows the mean annealing temperature of 423 °C for 10 minutes.

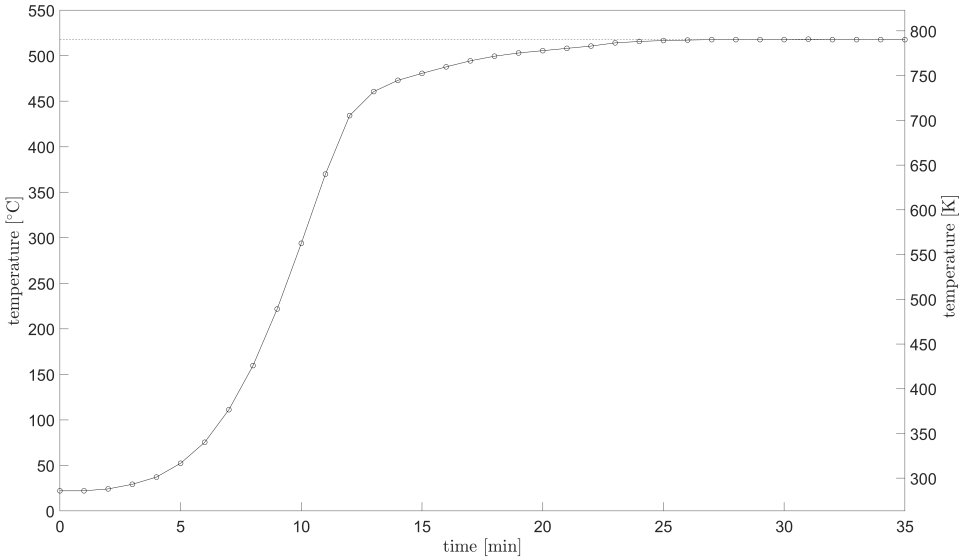

Figure 39: The fourth annealing stage of the VEP sample. The dotted line shows the mean annealing temperature of 518 °C for 10 minutes.

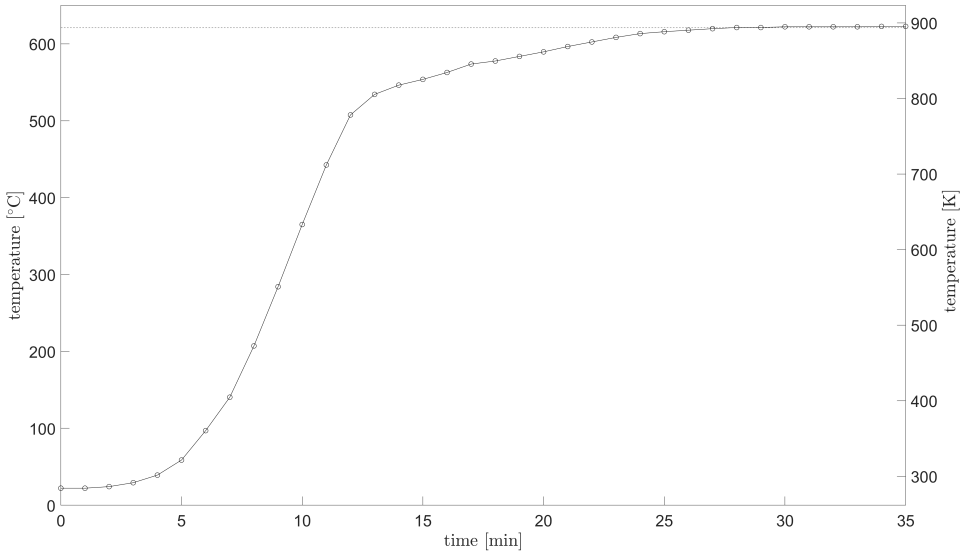

Figure 40: The fifth annealing stage of the VEP sample. The dotted line shows the mean annealing temperature of 620 °C for 10 minutes.

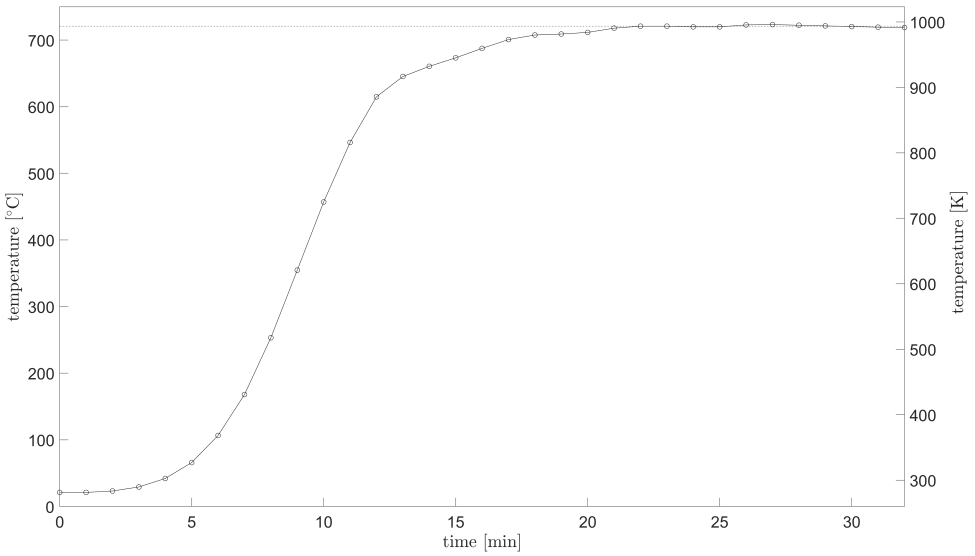

Figure 41: The sixth annealing stage of the VEP sample. The dotted line shows the mean annealing temperature of 721 °C for 10 minutes.

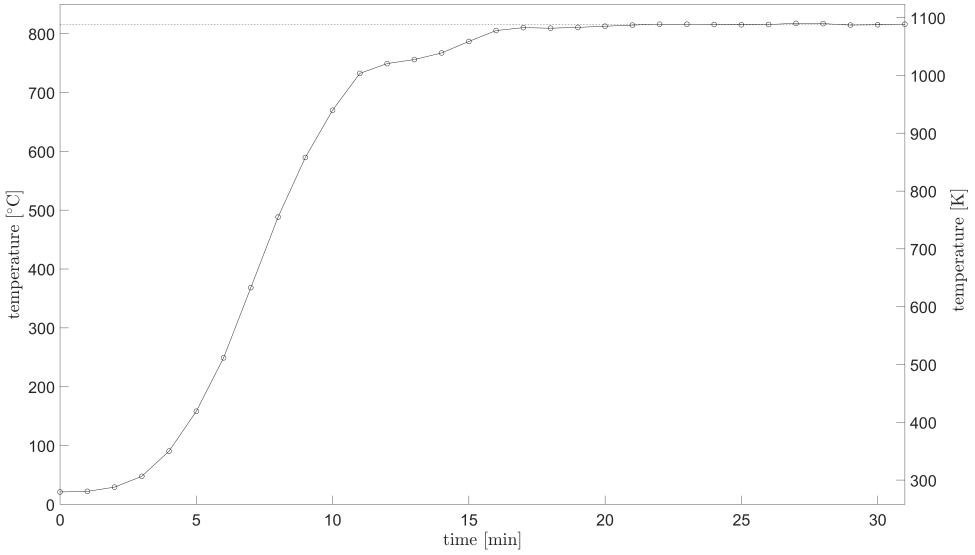

Figure 42: The seventh annealing stage of the VEP sample. The dotted line shows the mean annealing temperature of 816 °C for 10 minutes.

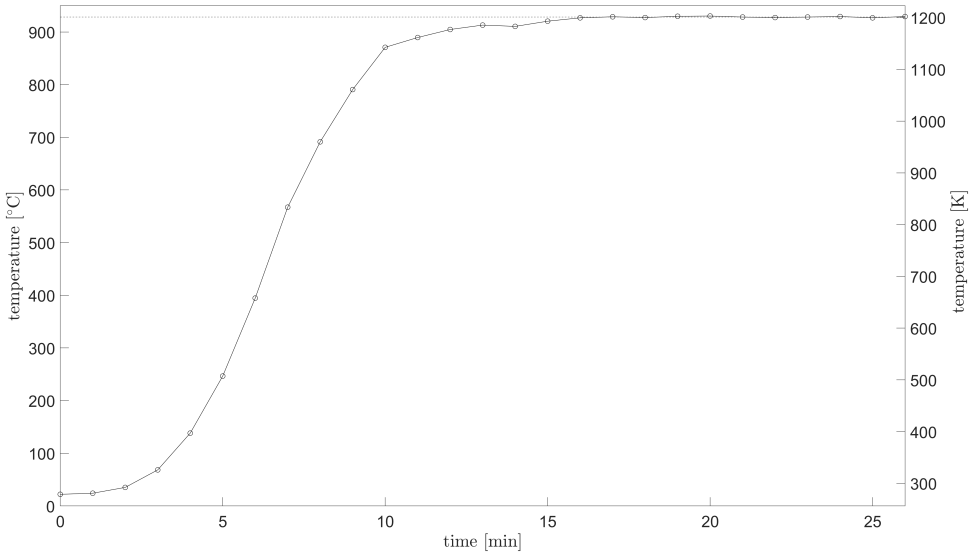

Figure 43: The eighth annealing stage of the VEP sample. The dotted line shows the mean annealing temperature of 928 °C for 10 minutes.

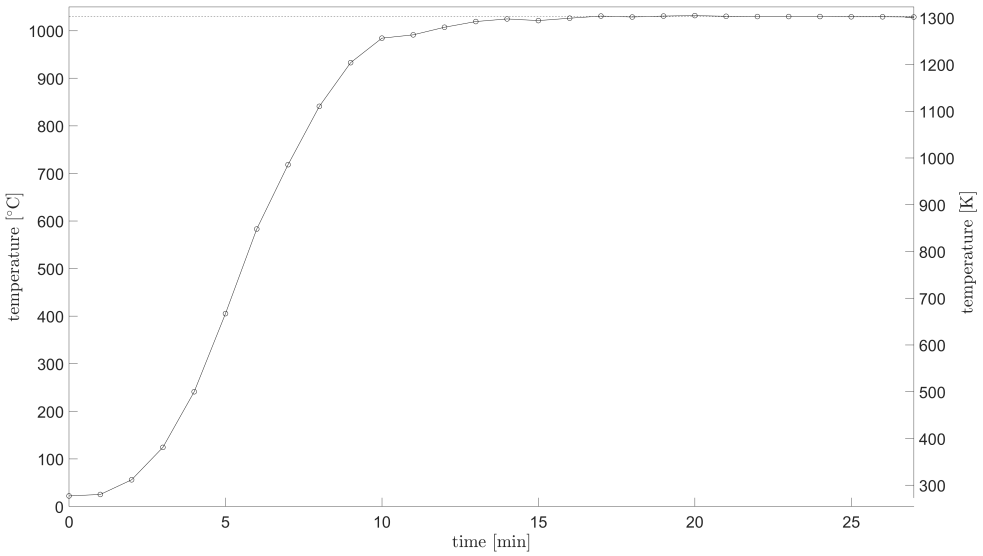

Figure 44: The ninth annealing stage of the VEP sample. The dotted line shows the mean annealing temperature of 1031 °C for 10 minutes.

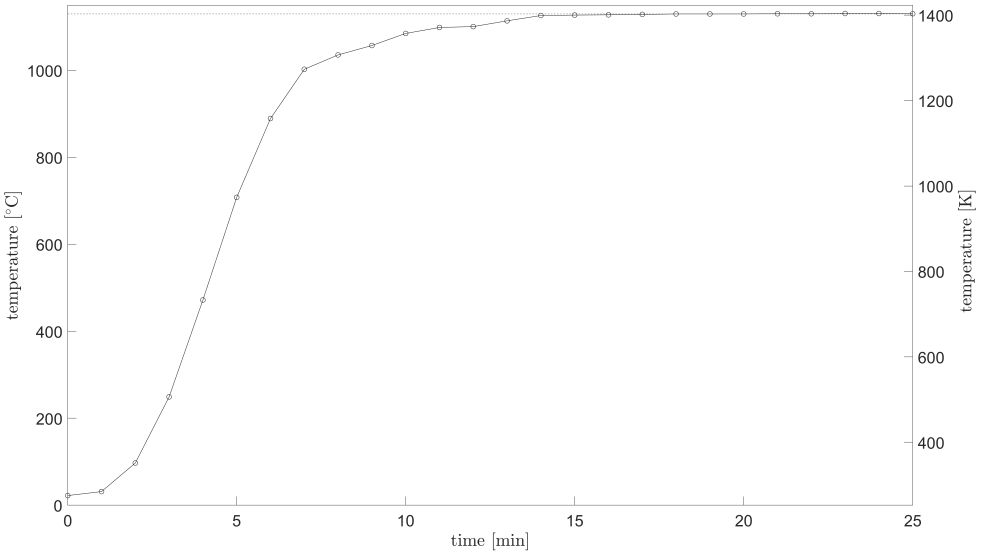

Figure 45: The tenth annealing stage of the VEP sample. The dotted line shows the mean annealing temperature of 1130 °C for 10 minutes.

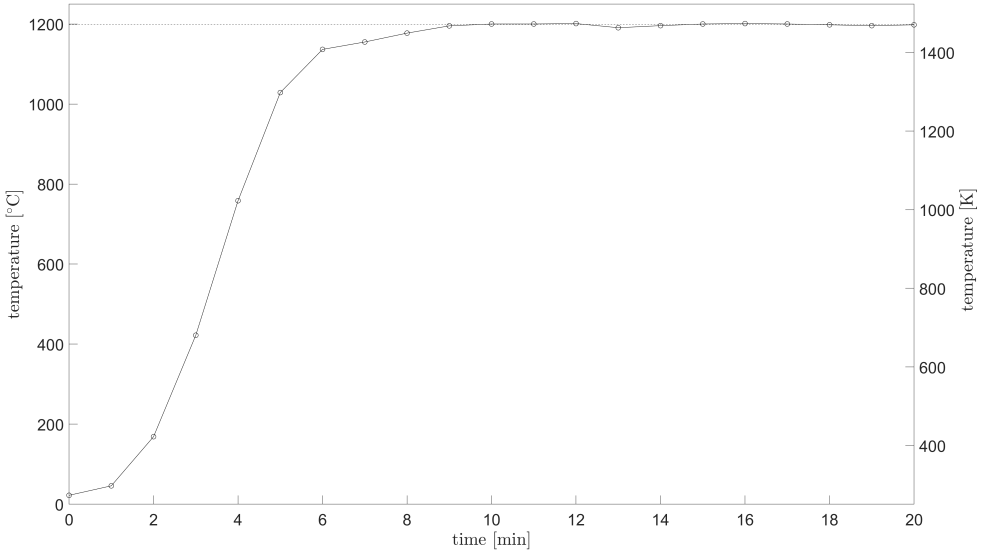

Figure 46: The eleventh annealing stage of the VEP sample. The dotted line shows the mean annealing temperature of 1199 °C for 10 minutes.

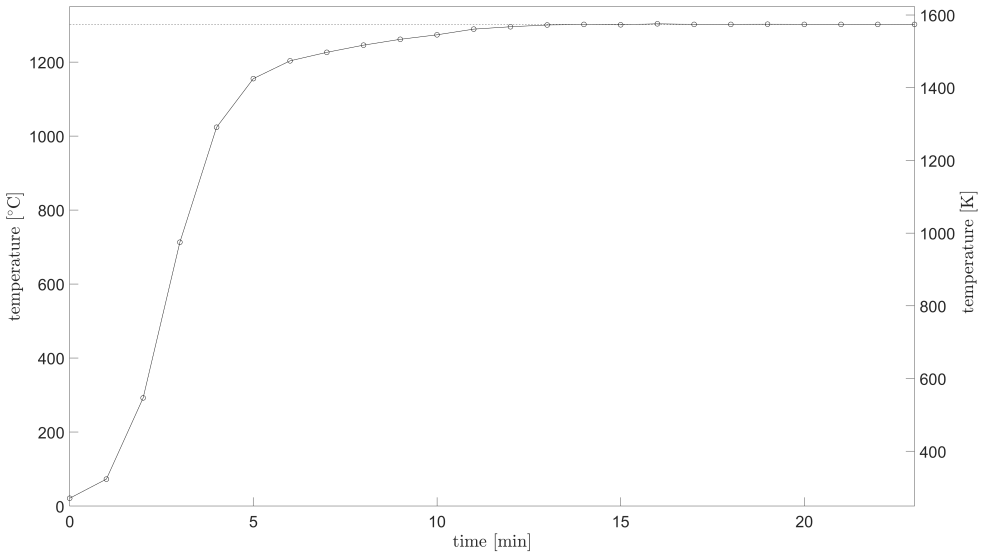

Figure 47: The twelfth annealing stage of the VEP sample. The dotted line shows the mean annealing temperature of 1302 °C for 10 minutes.

A.2 Hardness sample

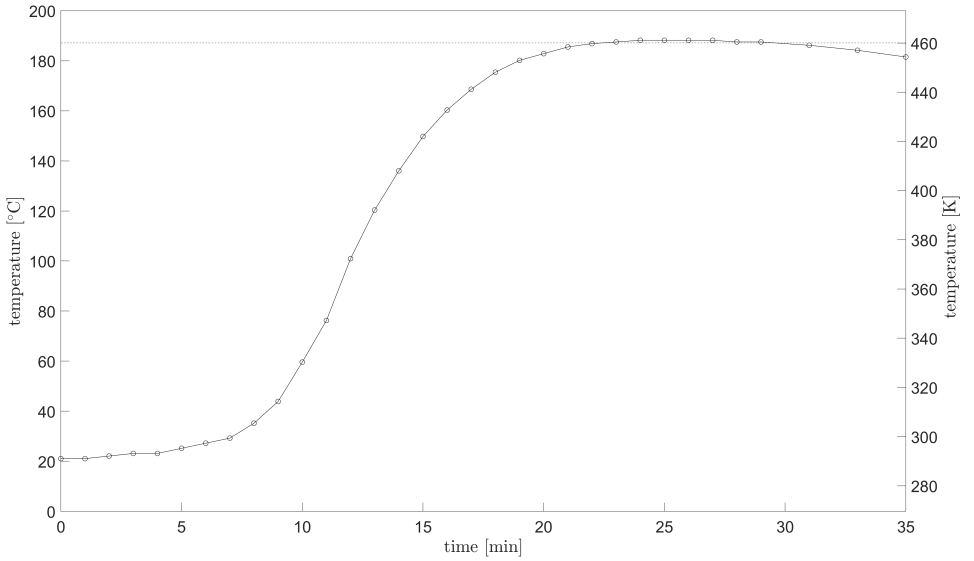

Figure 48: The first annealing stage of the hardness sample. The dotted line shows the mean annealing temperature of 187 °C for 10 minutes.

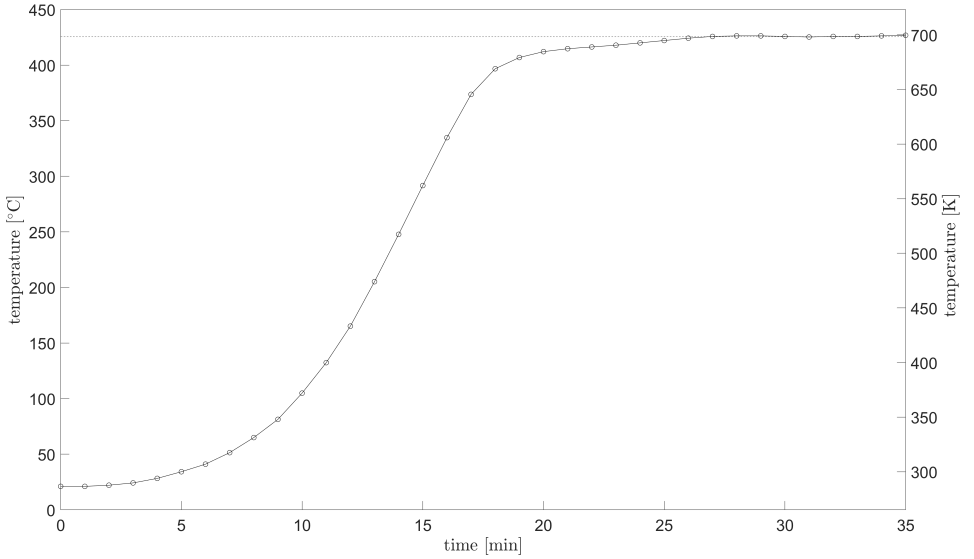

Figure 49: The second annealing stage of the hardness sample. The dotted line shows the mean annealing temperature of 426 °C for 10 minutes.

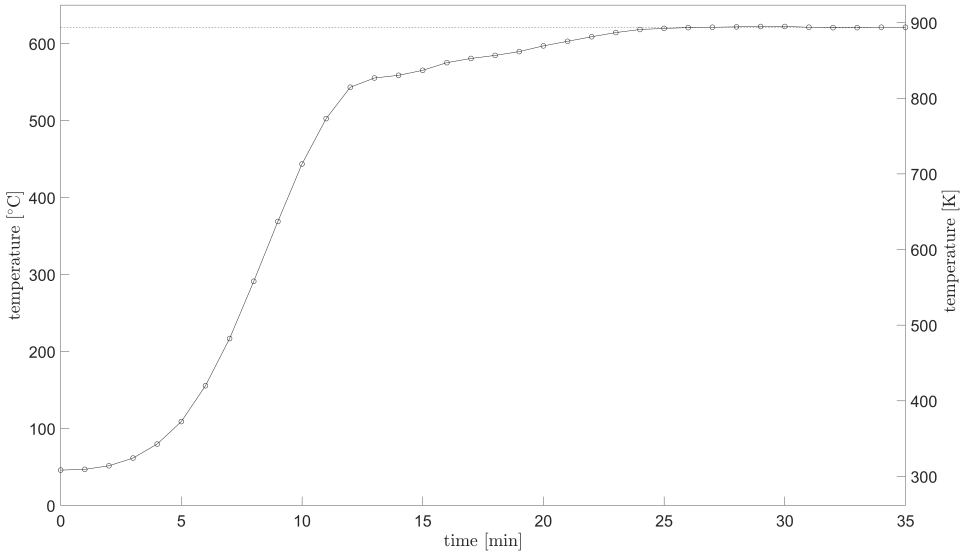

Figure 50: The third annealing stage of the hardness sample. The dotted line shows the mean annealing temperature of 621 °C for 10 minutes.

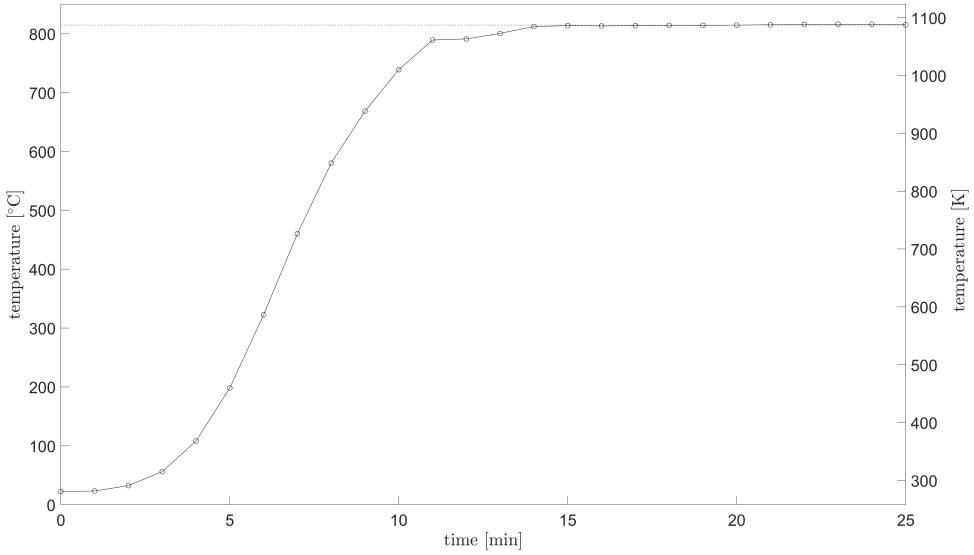

Figure 51: The fourth annealing stage of the hardness sample. The dotted line shows the mean annealing temperature of 815 °C for 10 minutes.

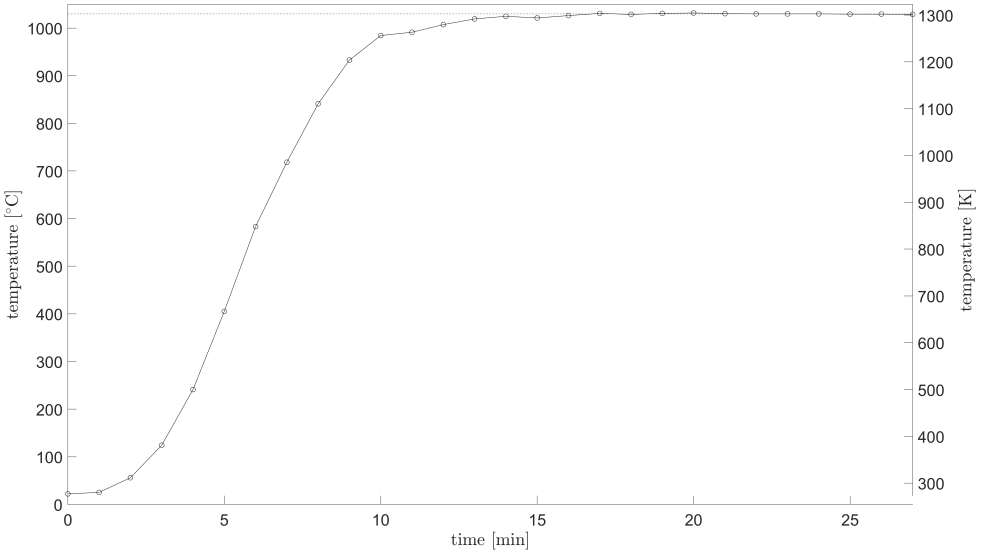

Figure 52: The fifth annealing stage of the hardness sample. The dotted line shows the mean annealing temperature of 1031 °C for 10 minutes.

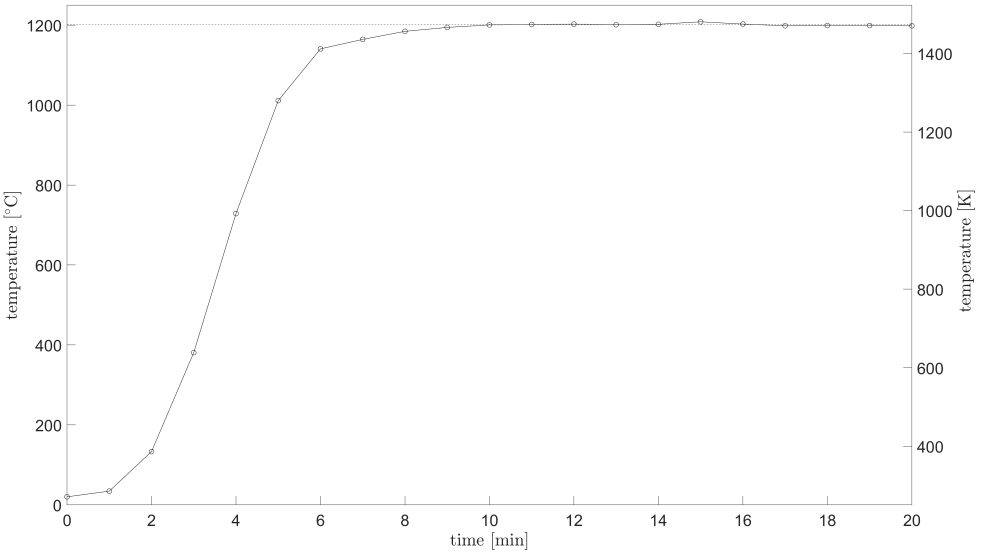

Figure 53: The sixth annealing stage of the hardness sample. The dotted line shows the mean annealing temperature of 1201 °C for 10 minutes.

A.3 Lifetime sample

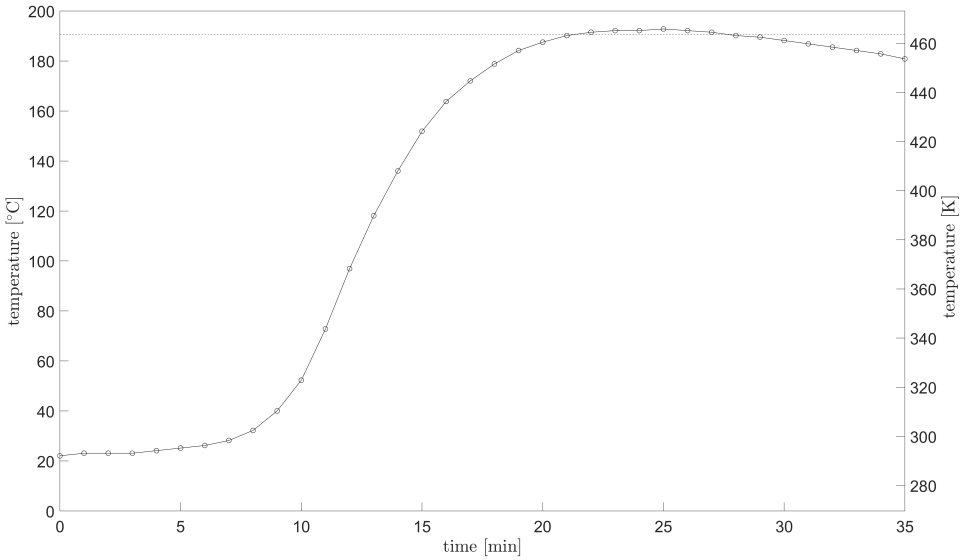

Figure 54: The first annealing stage of the lifetime sample. The dotted line shows the mean annealing temperature of 191 °C for 10 minutes.

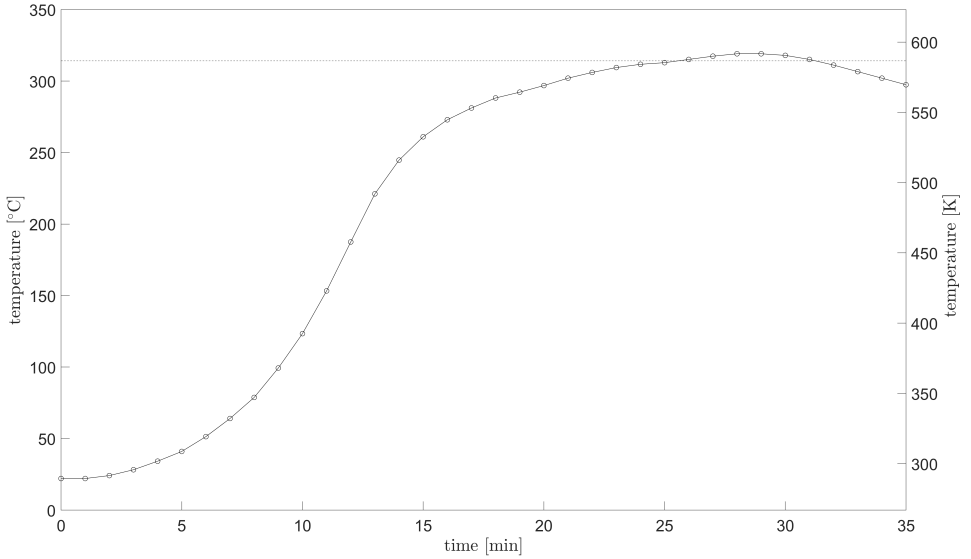

Figure 55: The second annealing stage of the lifetime sample. The dotted line shows the mean annealing temperature of 314 °C for 10 minutes.

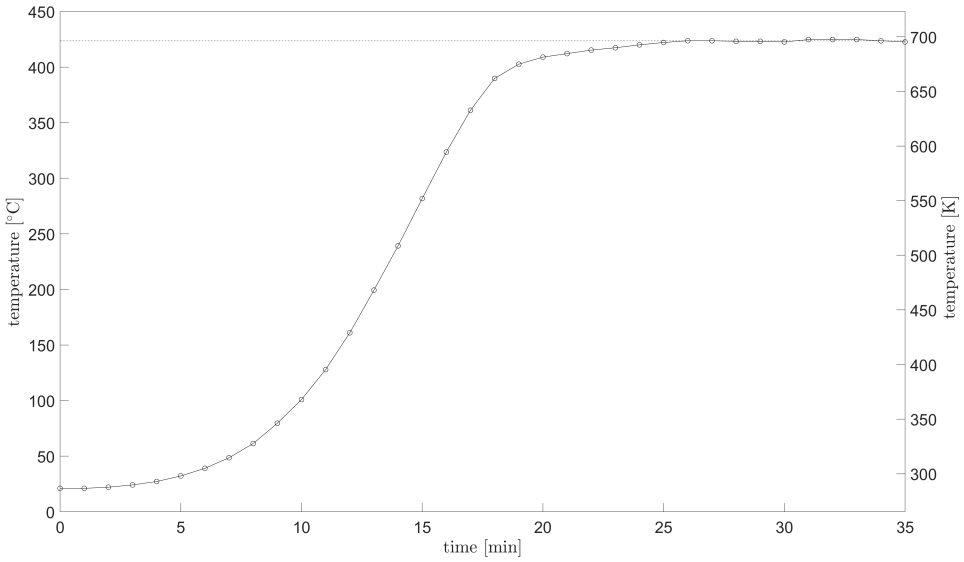

Figure 56: The third annealing stage of the lifetime sample. The dotted line shows the mean annealing temperature of 424 °C for 10 minutes.

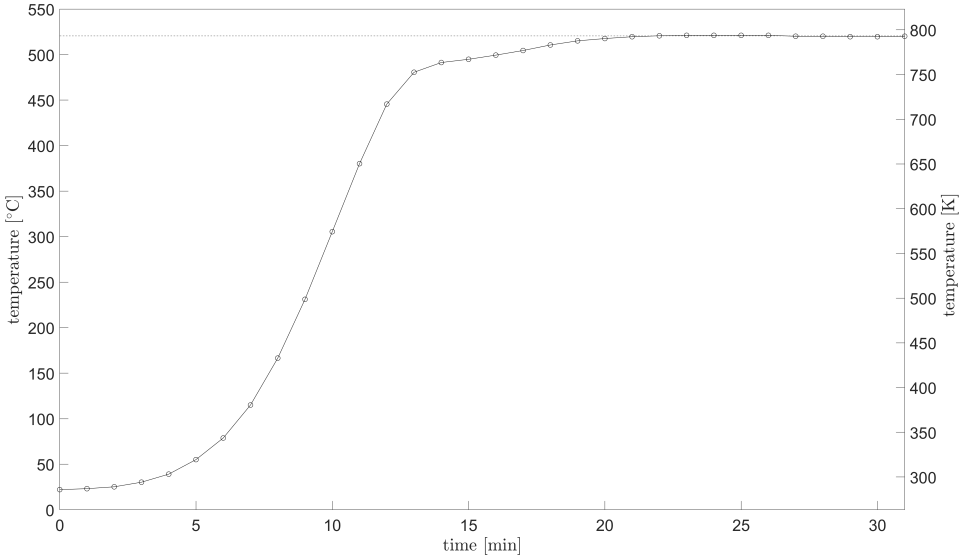

Figure 57: The fourth annealing stage of the lifetime sample. The dotted line shows the mean annealing temperature of 521 °C for 10 minutes.

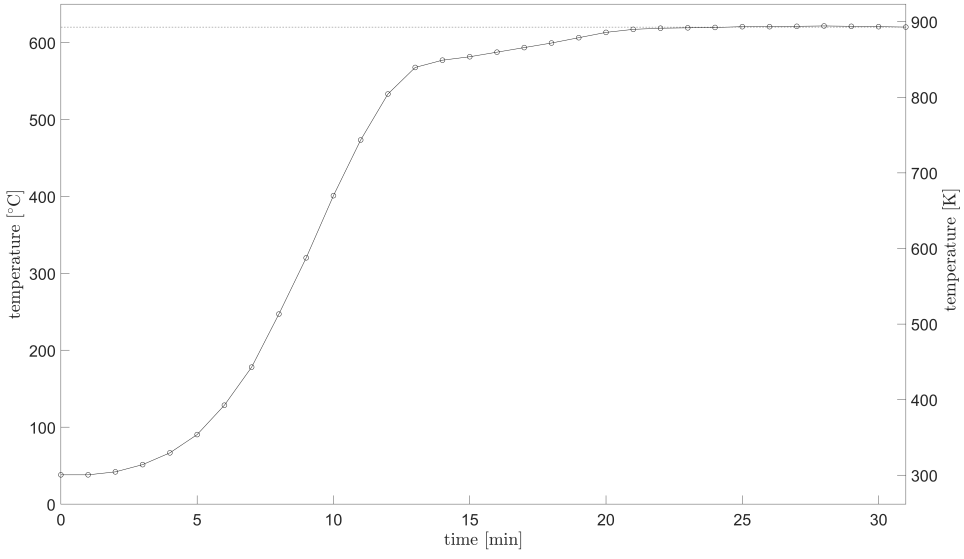

Figure 58: The fifth annealing stage of the lifetime sample. The dotted line shows the mean annealing temperature of 620 °C for 10 minutes.

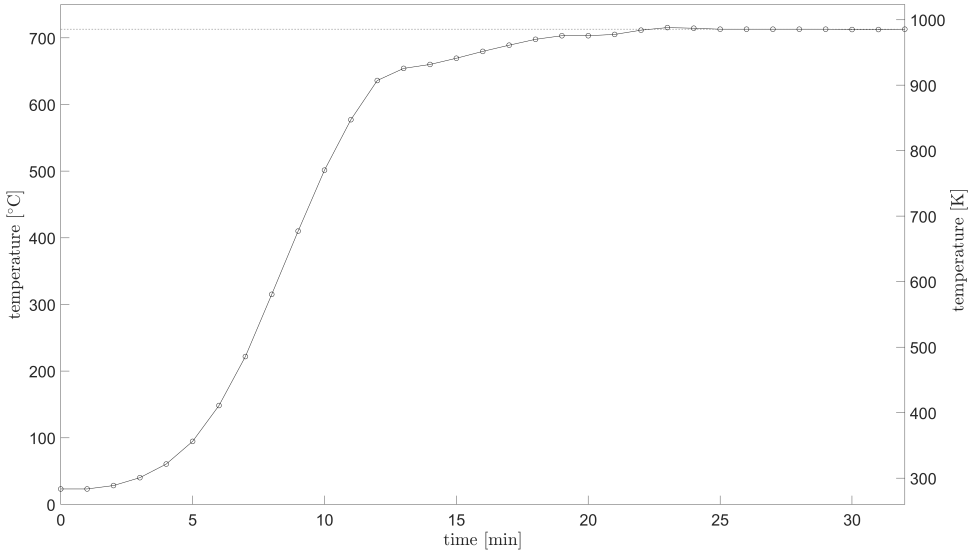

Figure 59: The sixth annealing stage of the lifetime sample. The dotted line shows the mean annealing temperature of 713 °C for 10 minutes.

Appendix B

VEPFIT plots

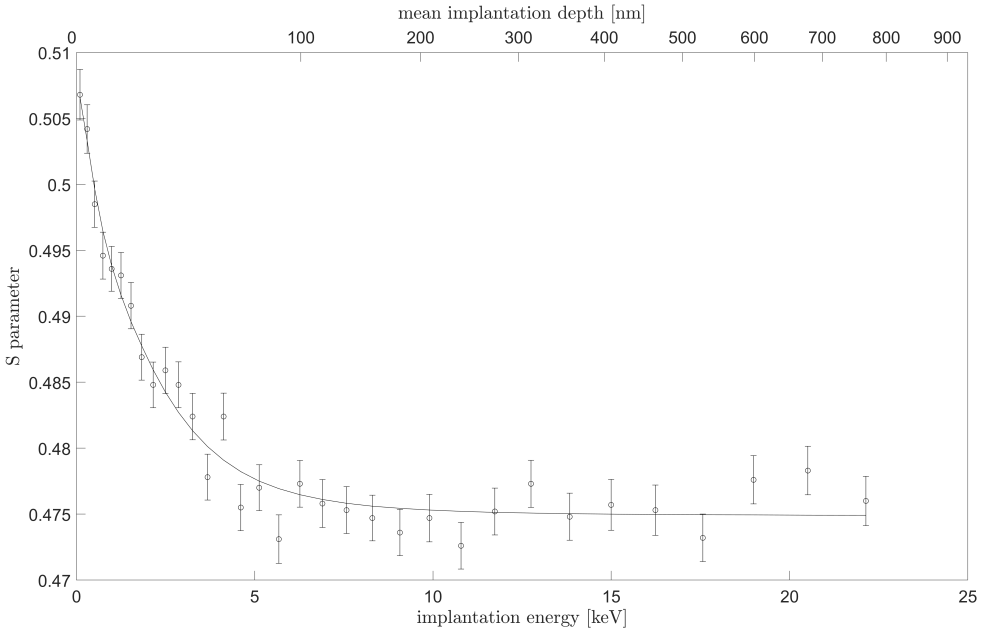

(a)

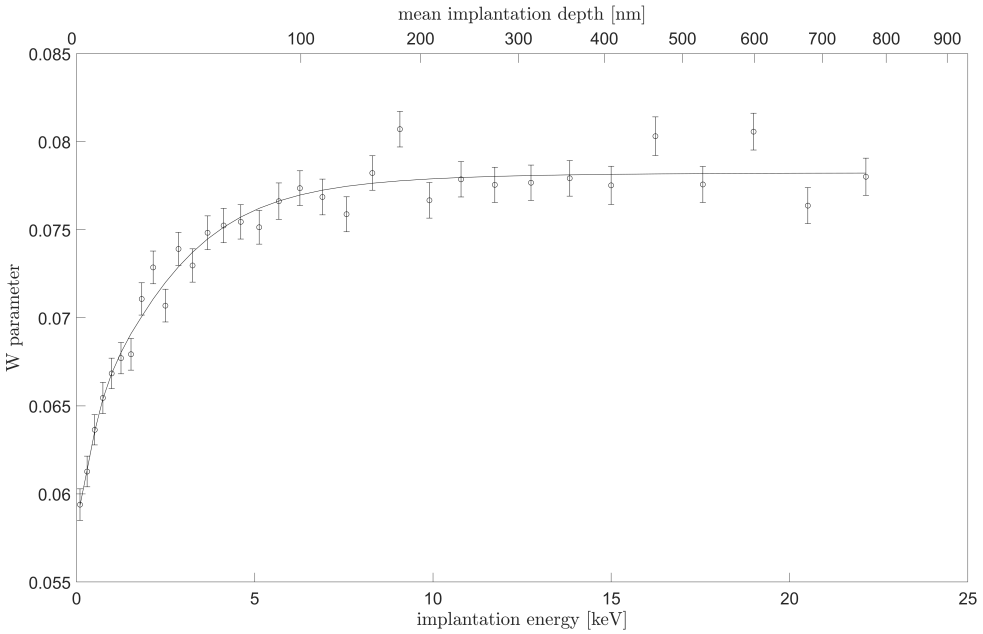

(b)

Figure 60: The results of the VEP measurement in the as received condition. In (a) and (b), respectively the S and W parameter are plotted against the implantation energy and the mean implantation depth. The fitted lines are the result of the VEPFIT software.

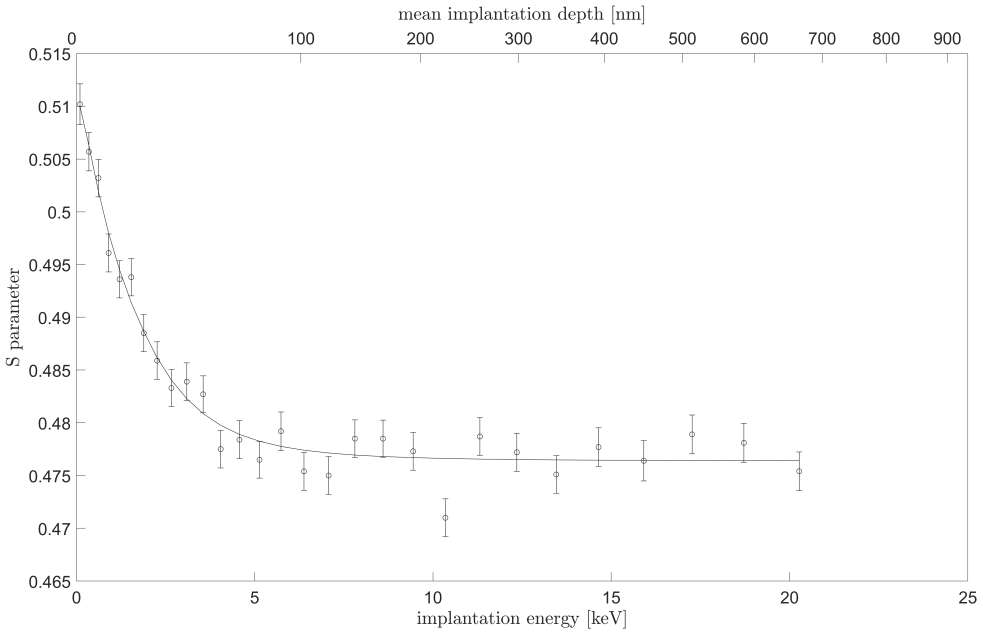

(a)

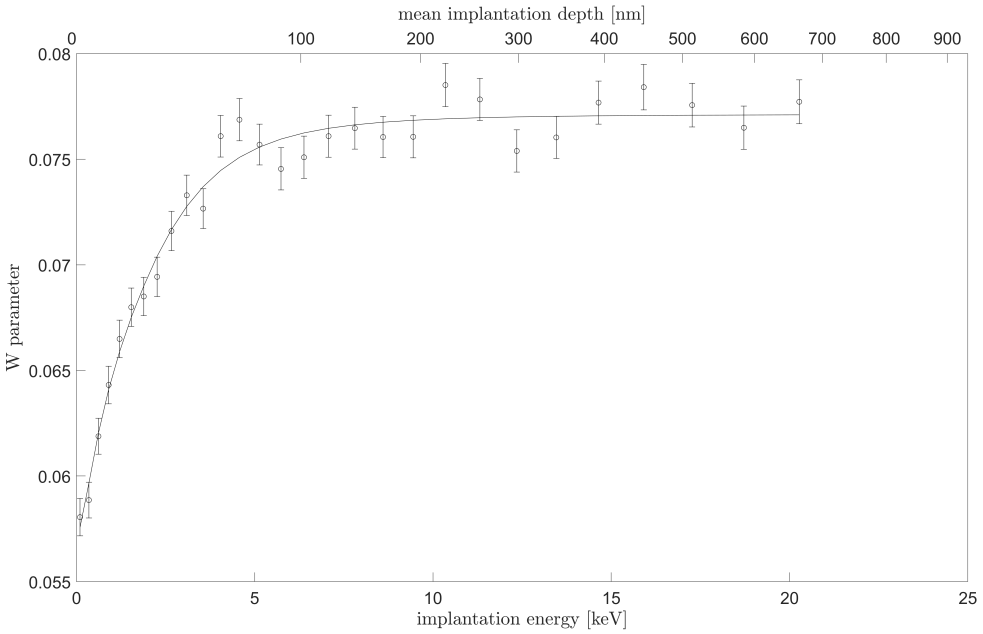

(b)

Figure 61: The results of the VEP measurement after annealing for 10 minutes at a mean temperature of 187 °C. In (a) and (b), respectively the S and W parameter are plotted against the implantation energy and the mean implantation depth. The fitted lines are the result of the VEPFIT software.

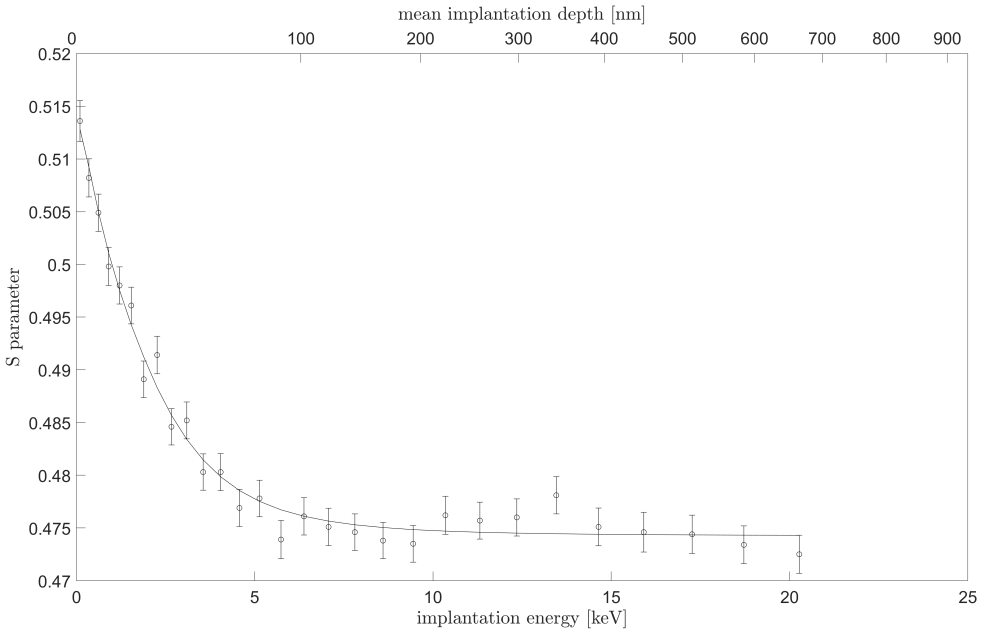

(a)

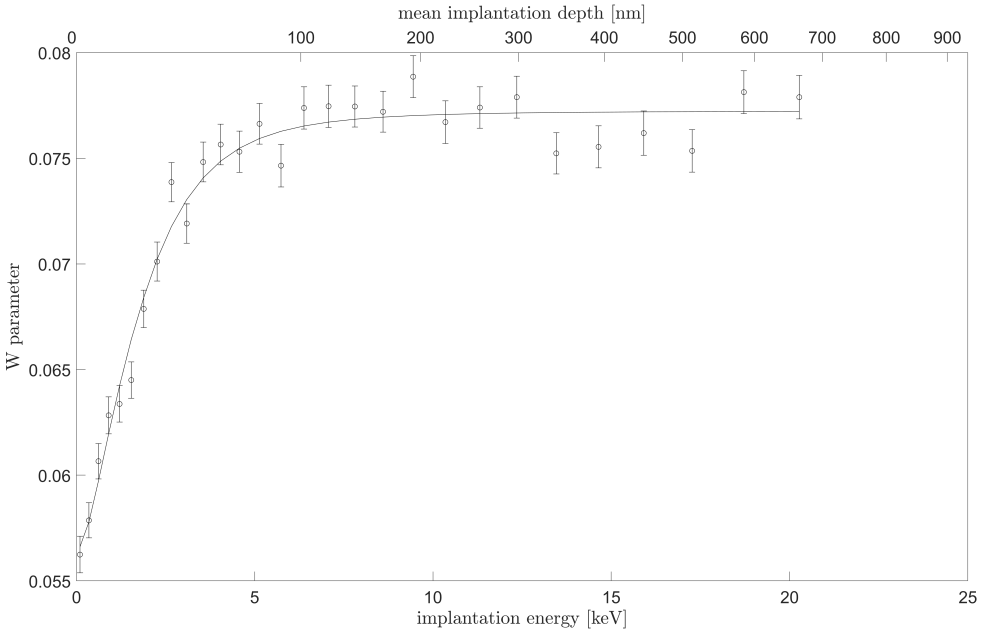

(b)

Figure 62: The results of the VEP measurement after annealing for 10 minutes at a mean temperature of 312 °C. In (a) and (b), respectively the S and W parameter are plotted against the implantation energy and the mean implantation depth. The fitted lines are the result of the VEPFIT software.

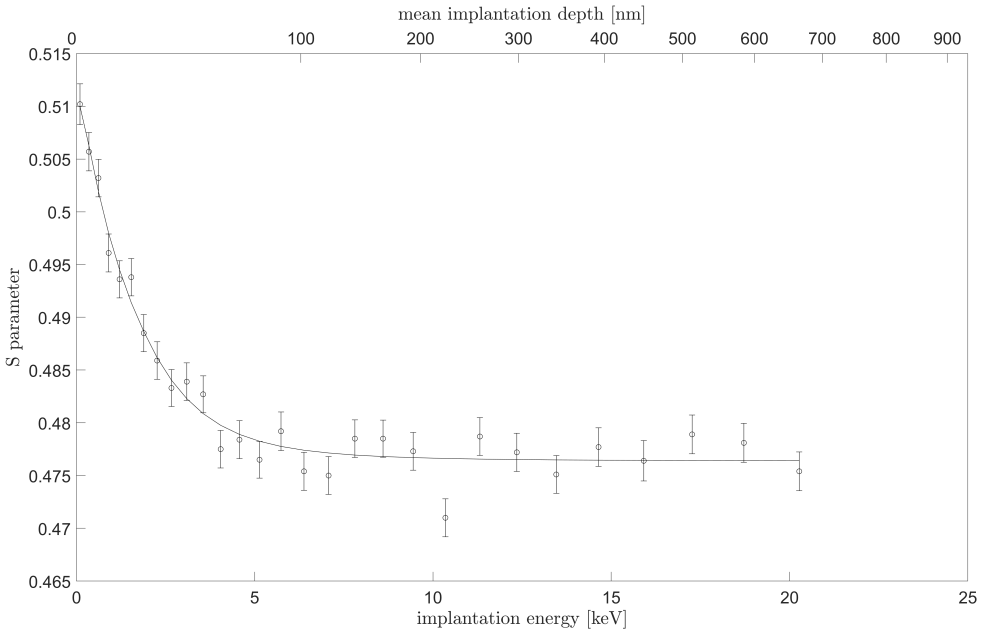

(a)

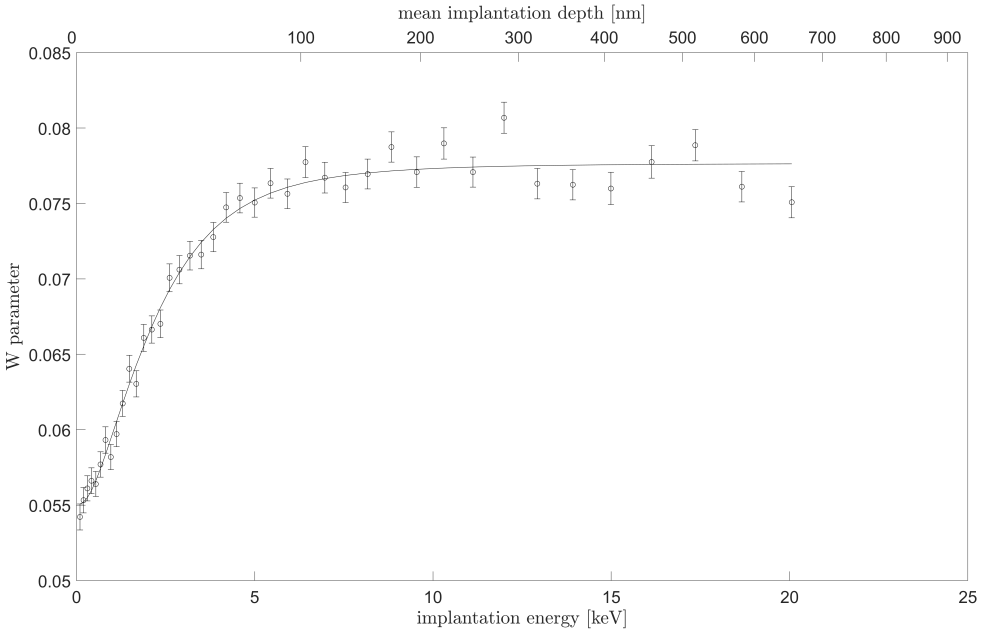

(b)

Figure 63: The results of the VEP measurement after annealing for 10 minutes at a mean temperature of 423 °C. In (a) and (b), respectively the S and W parameter are plotted against the implantation energy and the mean implantation depth. The fitted lines are the result of the VEPFIT software.

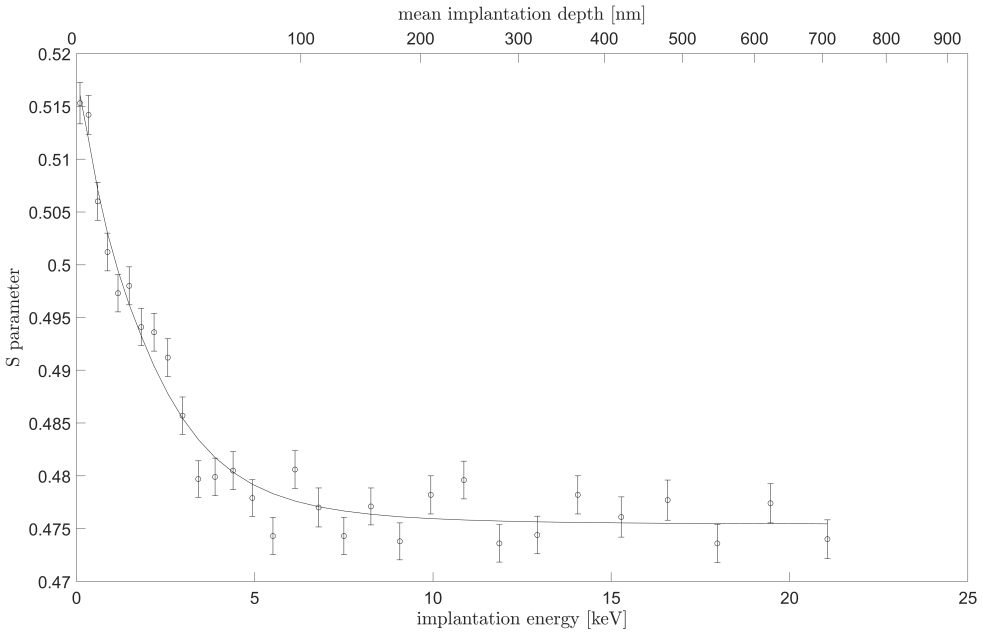

(a)

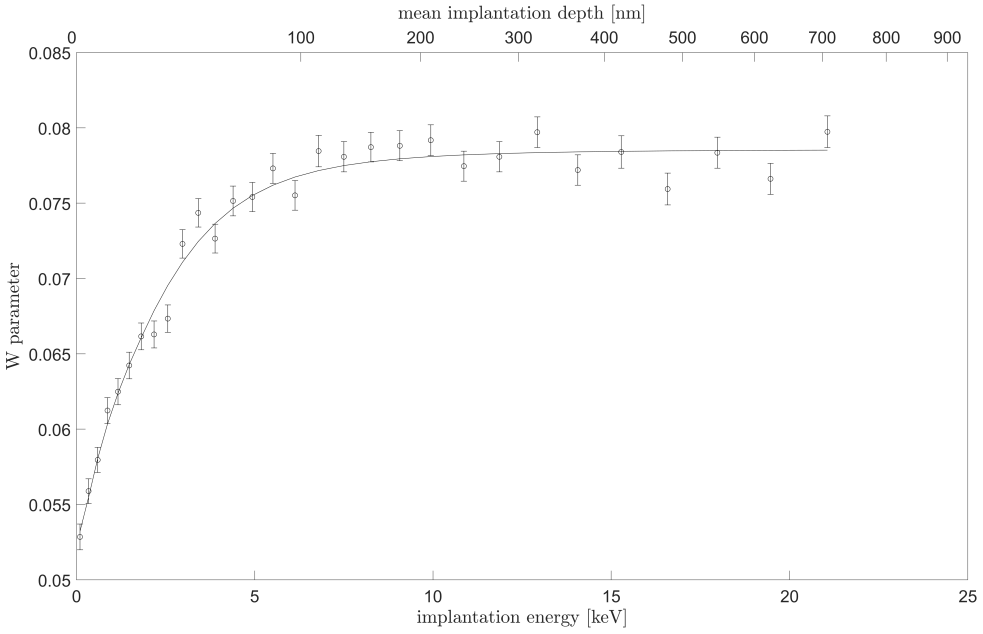

(b)

Figure 64: The results of the VEP measurement after annealing for 10 minutes at a mean temperature of 518 °C. In (a) and (b), respectively the S and W parameter are plotted against the implantation energy and the mean implantation depth. The fitted lines are the result of the VEPFIT software.

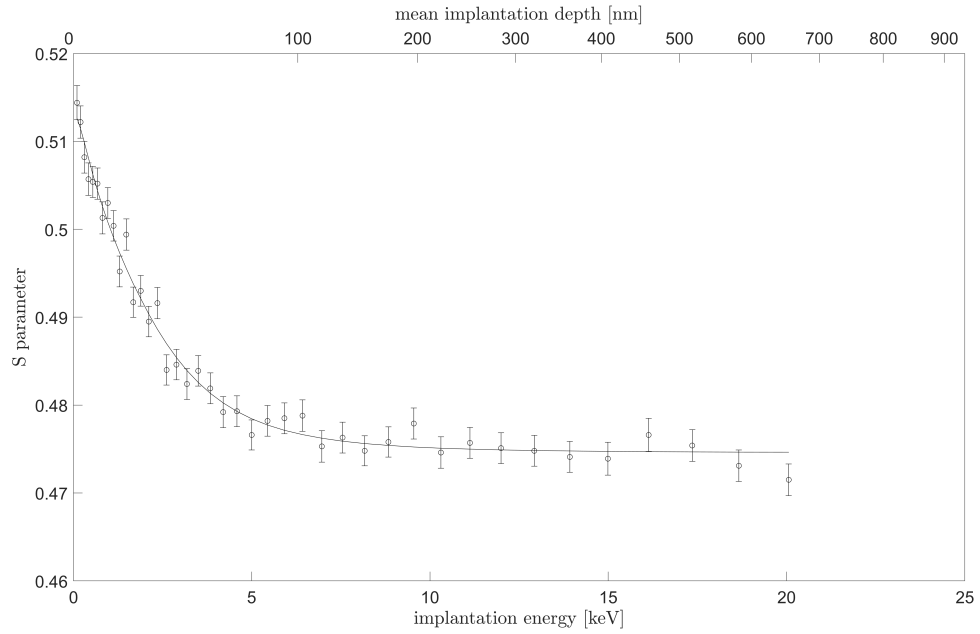

(a)

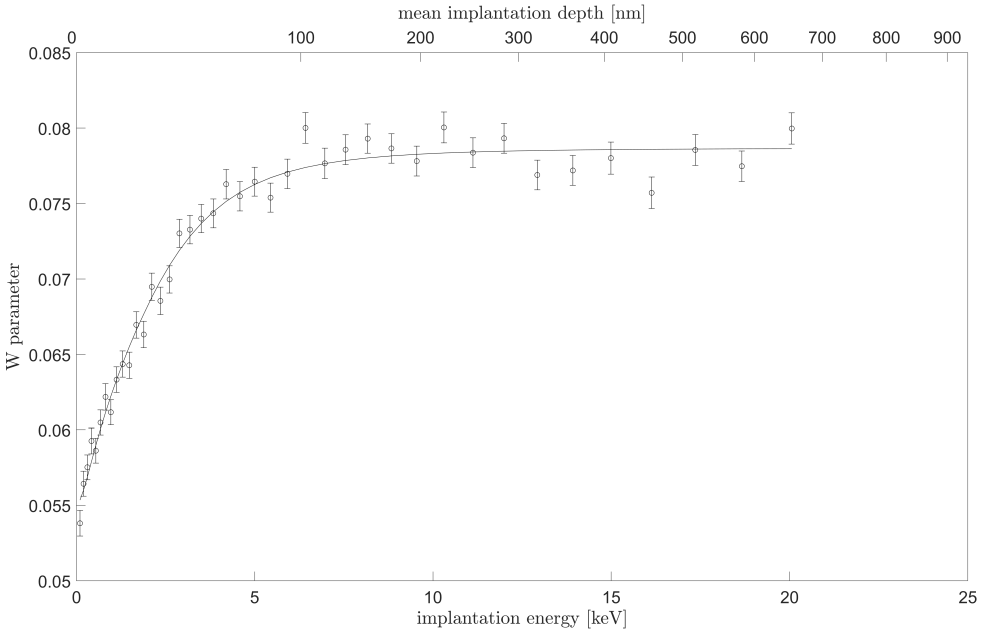

(b)

Figure 65: The results of the VEP measurement after annealing for 10 minutes at a mean temperature of 620 °C. In (a) and (b), respectively the S and W parameter are plotted against the implantation energy and the mean implantation depth. The fitted lines are the result of the VEPFIT software.

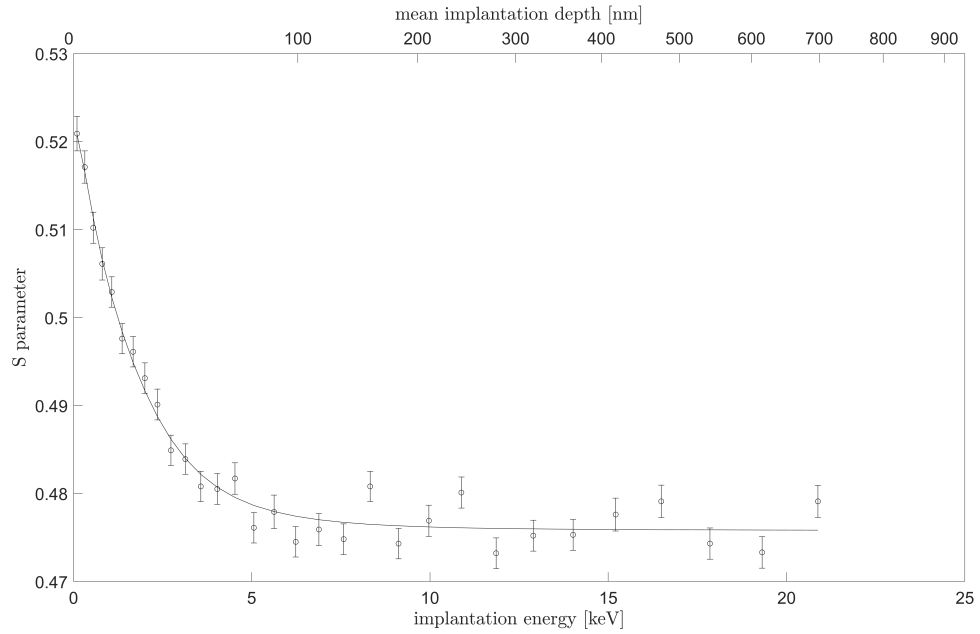

(a)

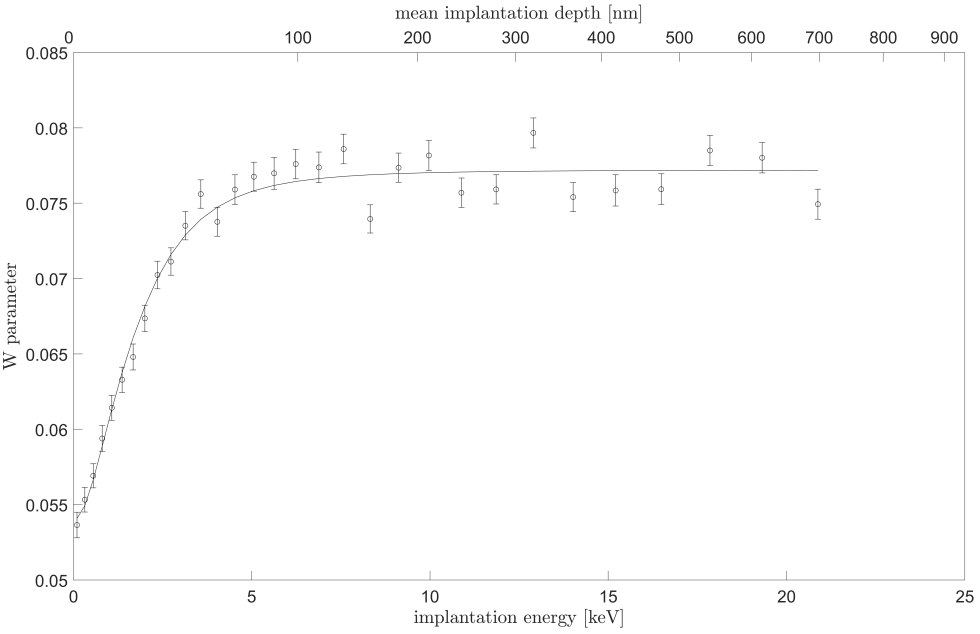

(b)

Figure 66: The results of the VEP measurement after annealing for 10 minutes at a mean temperature of 721 °C. In (a) and (b), respectively the S and W parameter are plotted against the implantation energy and the mean implantation depth. The fitted lines are the result of the VEPFIT software.

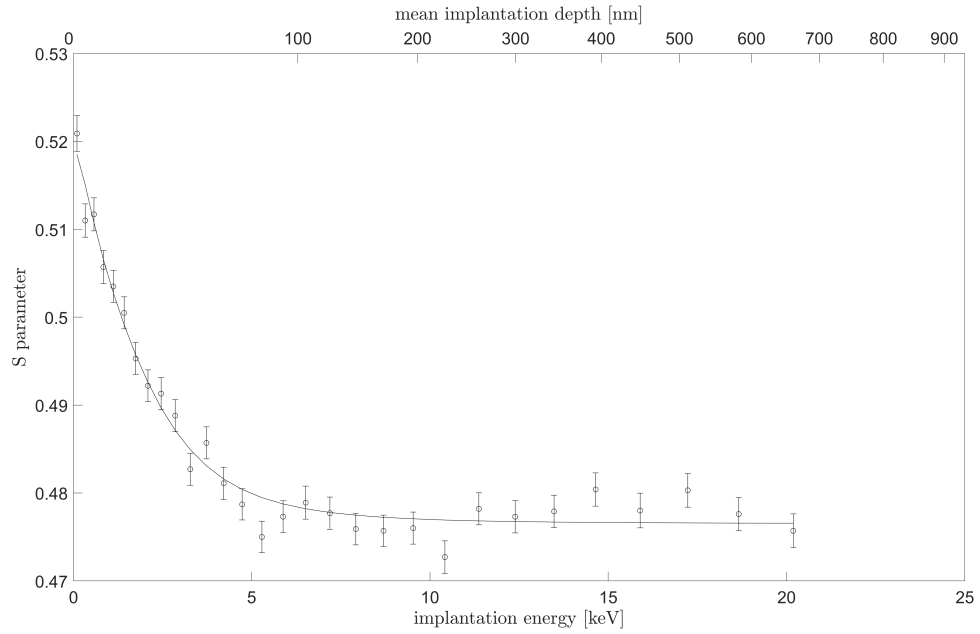

(a)

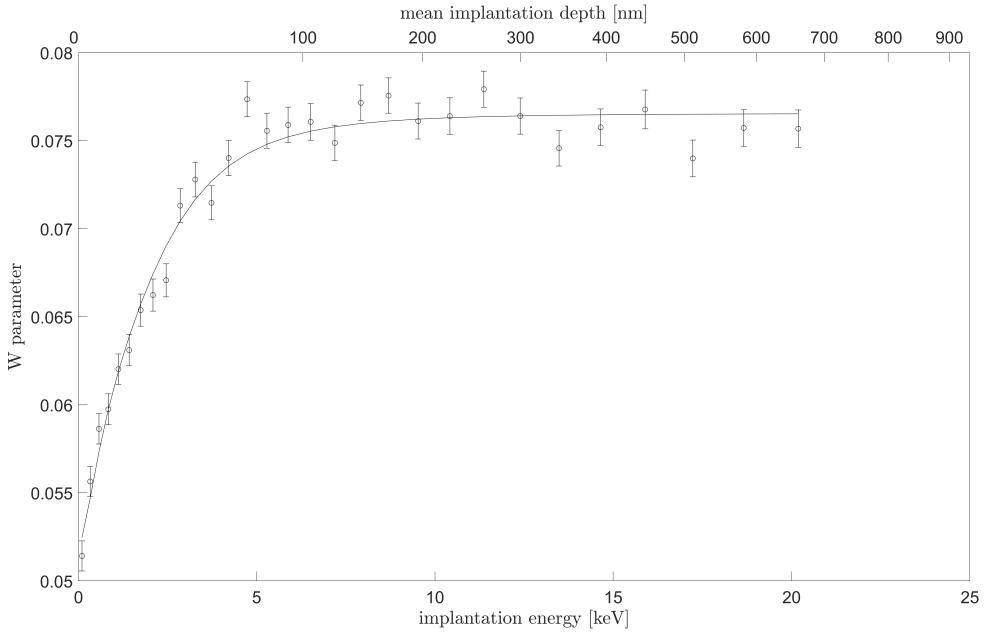

(b)

Figure 67: The results of the VEP measurement after annealing for 10 minutes at a mean temperature of 816 °C. In (a) and (b), respectively the S and W parameter are plotted against the implantation energy and the mean implantation depth. The fitted lines are the result of the VEPFIT software.

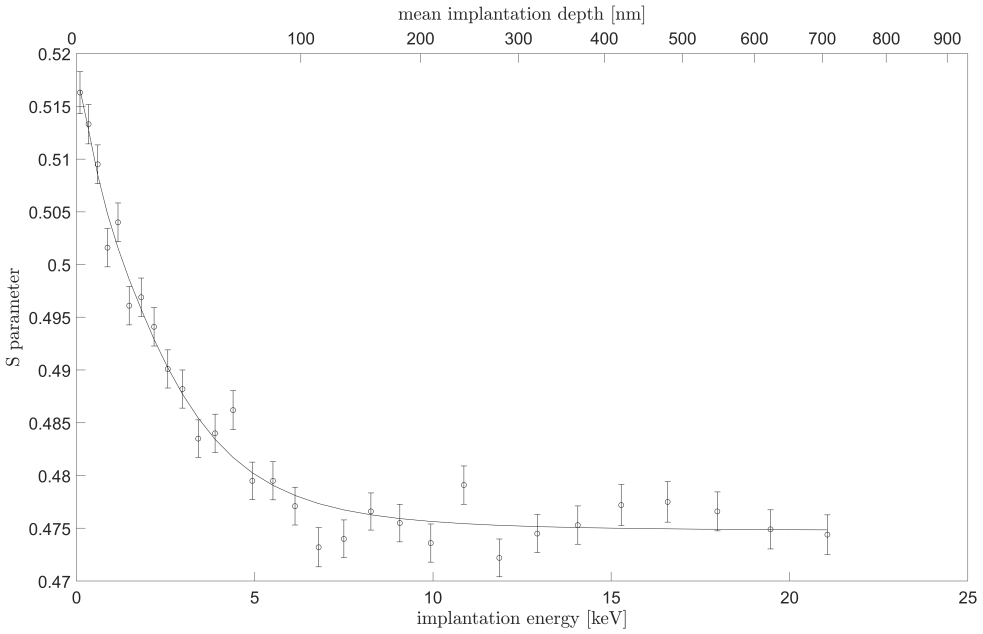

(a)

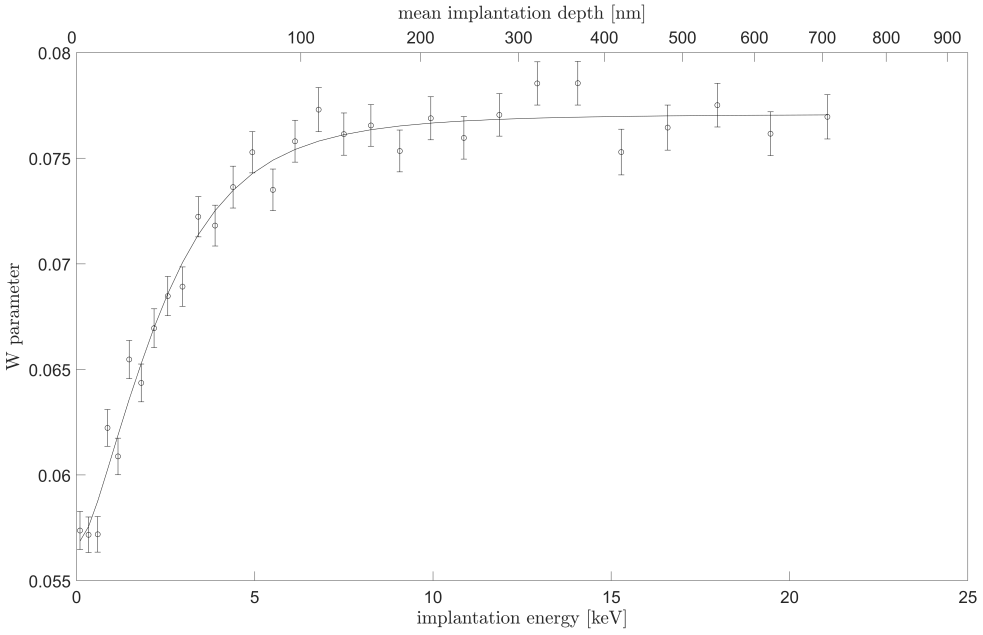

(b)

Figure 68: The results of the VEP measurement after annealing for 10 minutes at a mean temperature of 928 °C. In (a) and (b), respectively the S and W parameter are plotted against the implantation energy and the mean implantation depth. The fitted lines are the result of the VEPFIT software.

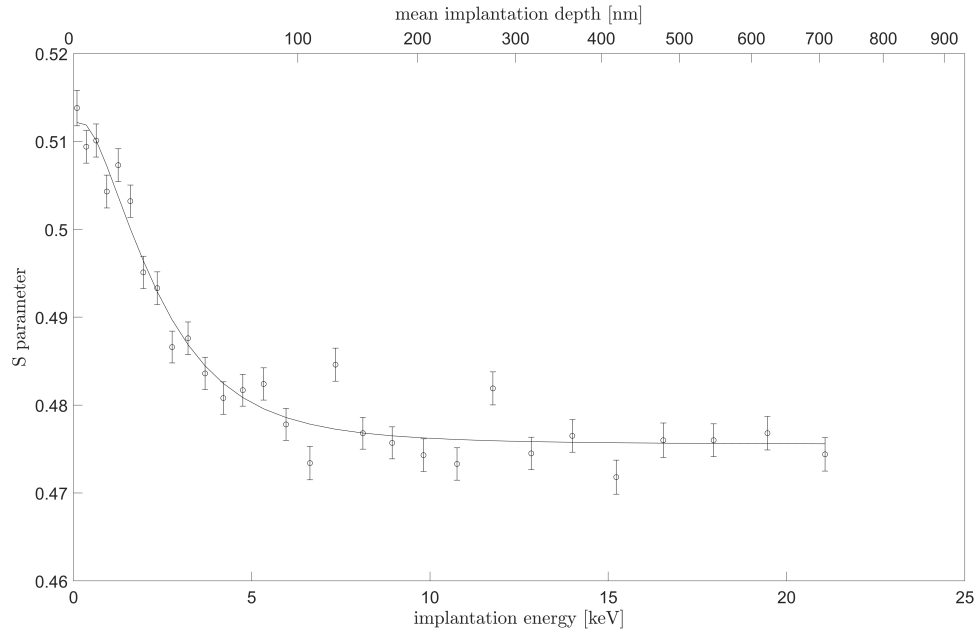

(a)

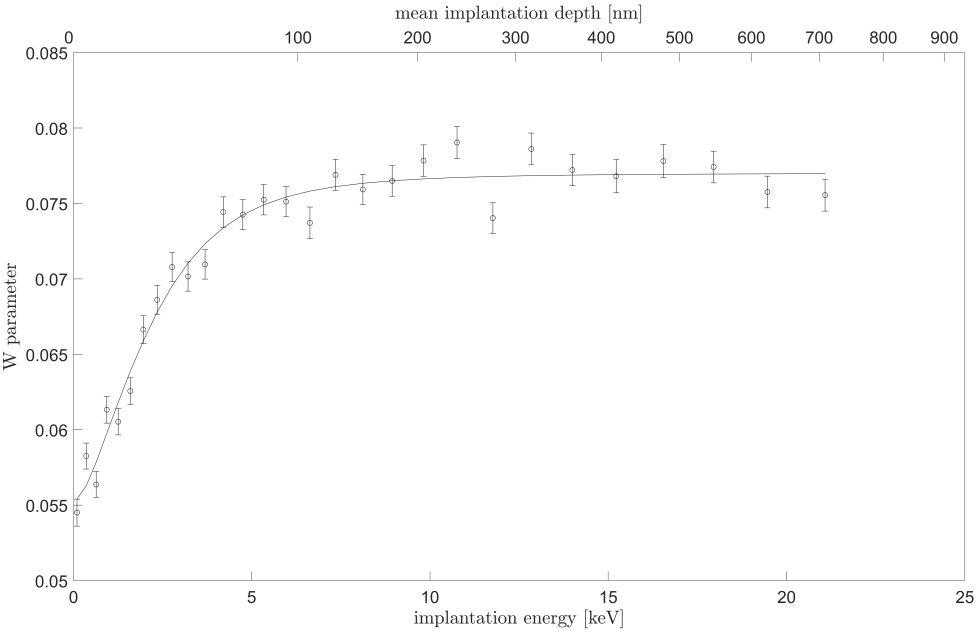

(b)

Figure 69: The results of the VEP measurement after annealing for 10 minutes at a mean temperature of 1031 °C. In (a) and (b), respectively the S and W parameter are plotted against the implantation energy and the mean implantation depth. The fitted lines are the result of the VEPFIT software.

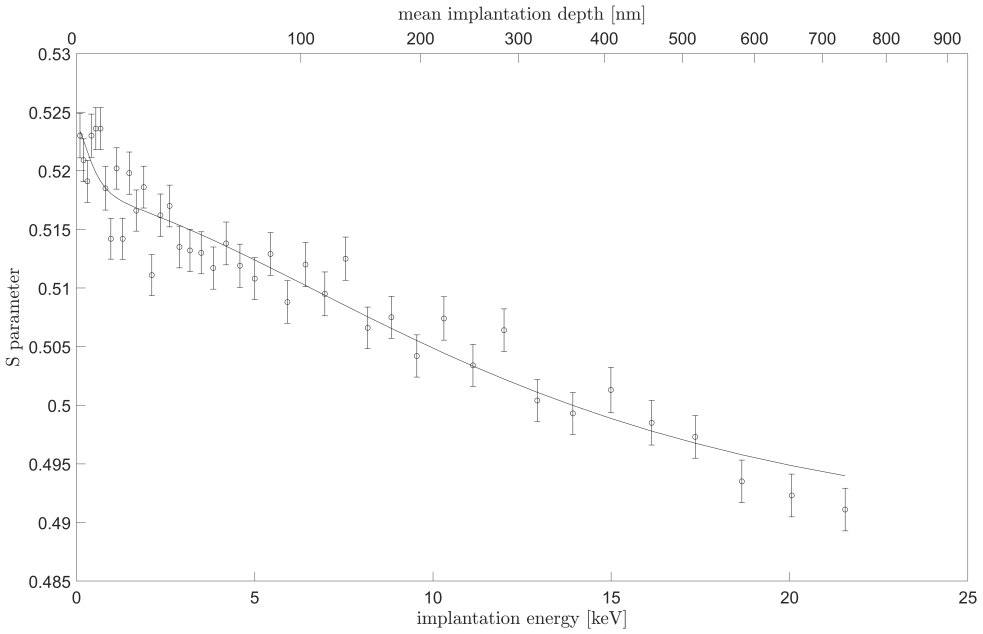

(a)

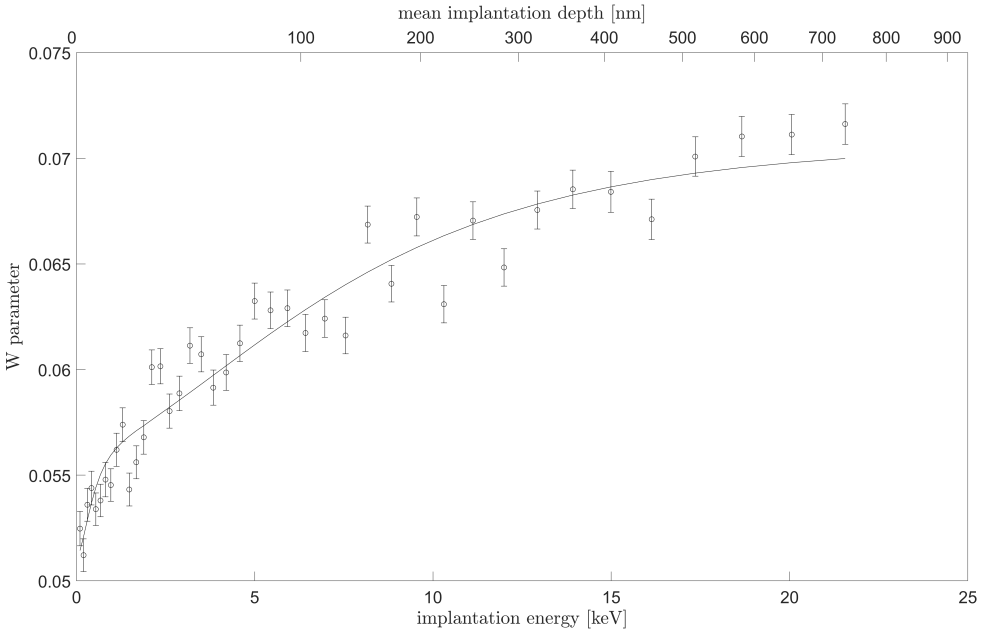

(b)

Figure 70: The results of the VEP measurement after annealing for 10 minutes at a mean temperature of 1130 °C. In (a) and (b), respectively the S and W parameter are plotted against the implantation energy and the mean implantation depth. The fitted lines are the result of the VEPFIT software.

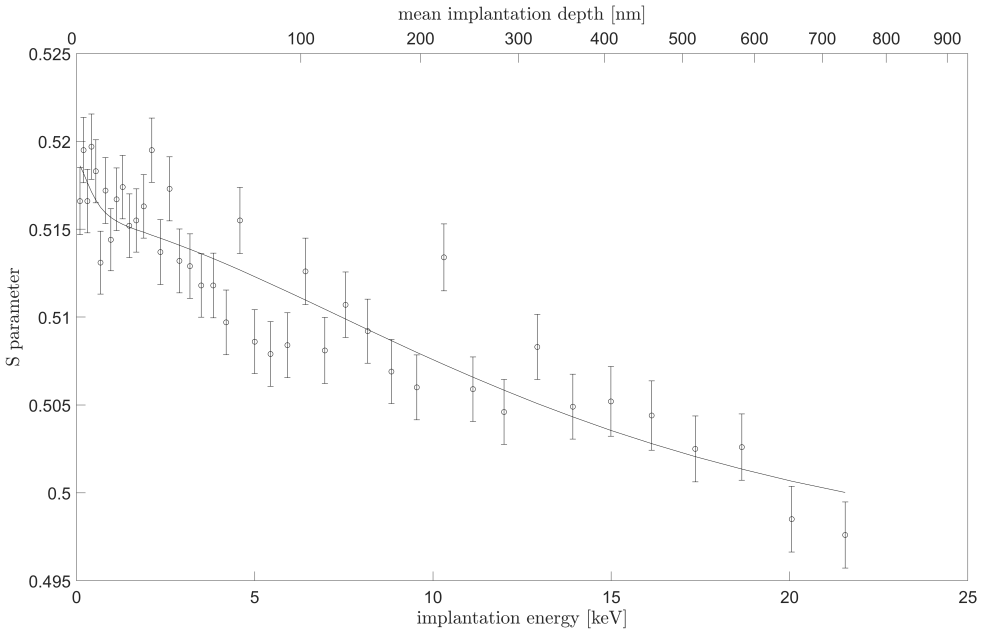

(a)

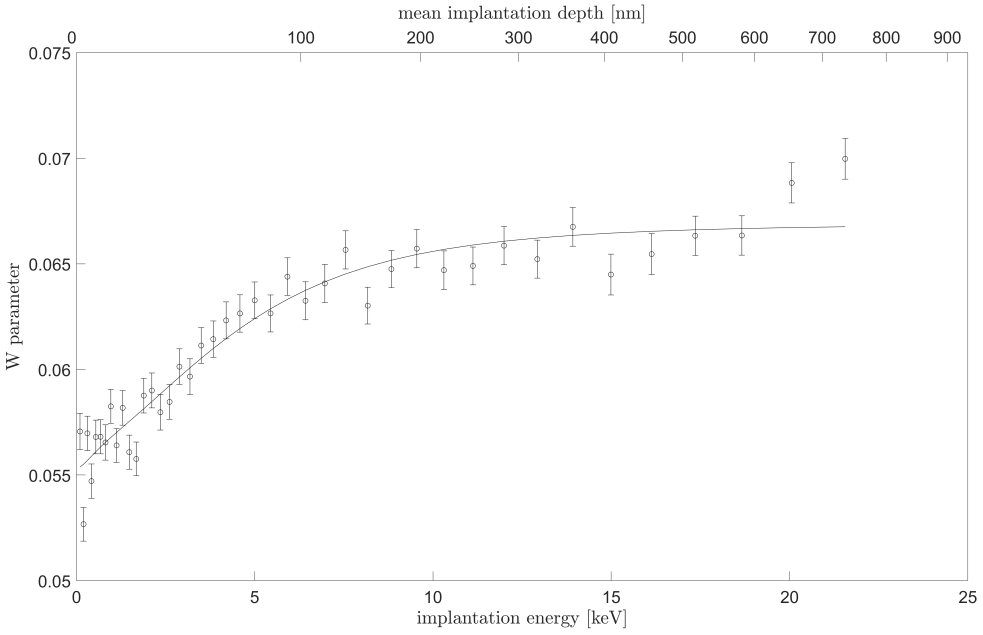

(b)

Figure 71: The results of the VEP measurement after annealing for 10 minutes at a mean temperature of 1199 °C. In (a) and (b), respectively the S and W parameter are plotted against the implantation energy and the mean implantation depth. The fitted lines are the result of the VEPFIT software.

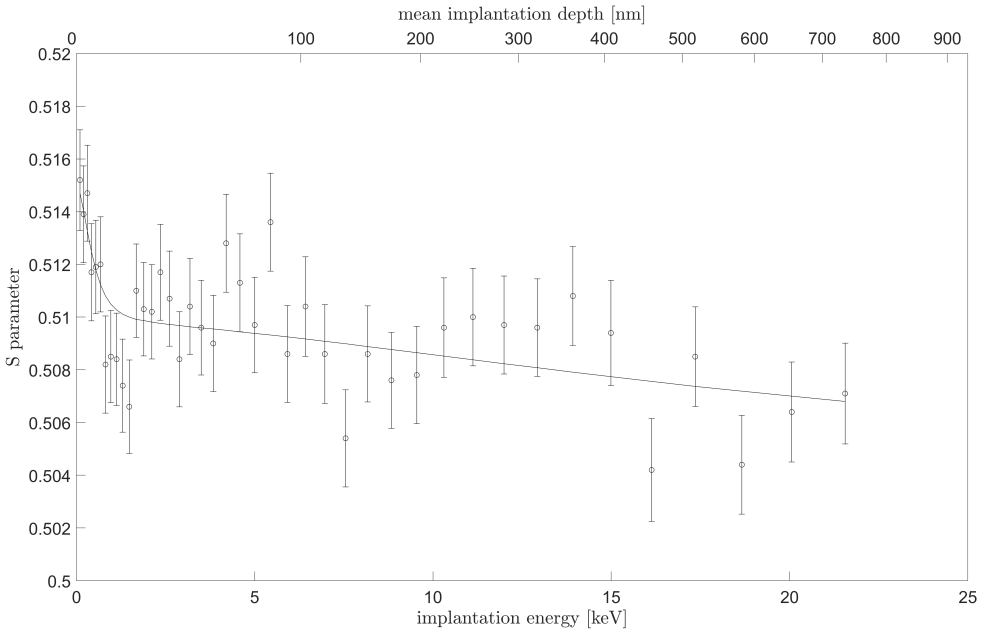

(a)

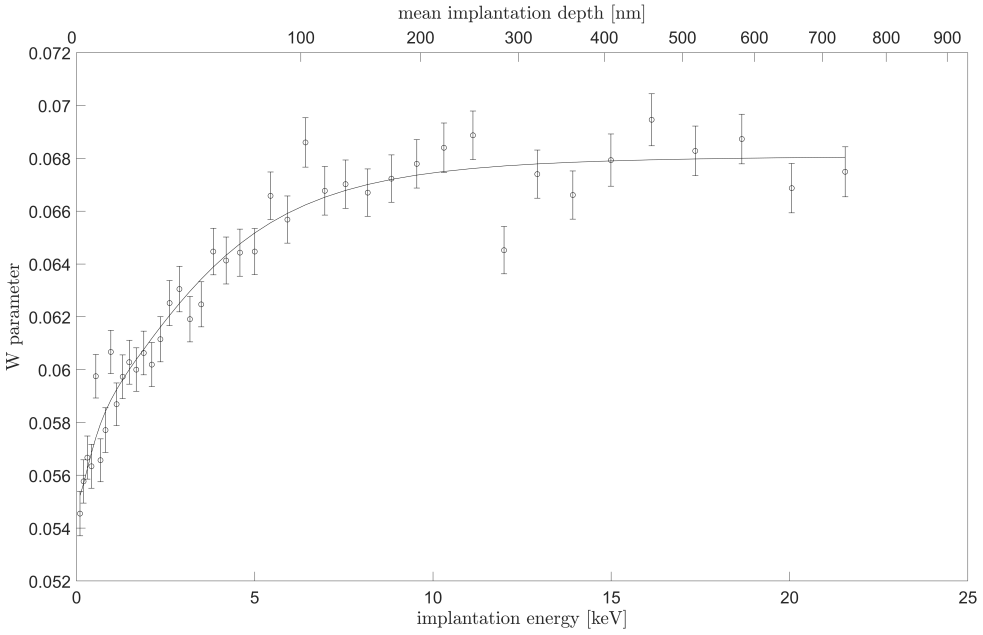

(b)

Figure 72: The results of the VEP measurement after annealing for 10 minutes at a mean temperature of 1302 °C. In (a) and (b), respectively the S and W parameter are plotted against the implantation energy and the mean implantation depth. The fitted lines are the result of the VEPFIT software.